## Title

InSAR-based detection method for mapping and monitoring slow-moving landslides in remote regions with steep and mountainous terrain: An application to Nepal



## Authors

Bekaert, David PS
Handwerger, Alexander L
Agram, Piyush
et al.

## Publication Date

2020-11-01

## DOI

10.1016/j.rse.2020.111983

# InSAR-based detection method for mapping and monitoring slow-moving landslides in remote regions with steep and mountainous terrain: An application to Nepal

## Highlights

- A novel method is developed to detect landslides in mountainous terrain
- InSAR time-series is used to identify and monitor slow-moving landslides
- 6 slow-moving landslides in Trishuli, Nepal, unaffected by the Gorkha earthquake
- Landslides have rates between 2-9 cm/yr and likely driven by monsoonal rainfall


**Authors and Affiliations:**

[a]David P.S. Bekaert, David.Bekaert@jpl.nasa.gov,

[a,b]Alexander L. Handwerger, alexander.handwerger@jpl.nasa.gov,

[a]Piyush Agram, piyush.agram@jpl.nasa.gov,

[c]Dalia B. Kirschbaum, dalia.b.kirschbaum@nasa.gov,

[a]Jet Propulsion Laboratory, California Institute of Technology, Pasadena, CA, USA

[b]Joint Institute for Regional Earth System Science and Engineering, University of California, Los Angeles, CA, USA.

[c]Hydrological Sciences Laboratory, NASA Goddard Space Flight Center, Greenbelt, MD, USA,



**Keywords:**

Synthetic Aperture Radar, Time-series InSAR

Detection,

Slow-moving landslide, Deep-seated landslide

Earthquake, Gorkha Earthquake

Trishuli

# Abstract

Mapping and monitoring landslides in remote areas with steep and mountainous terrain is logistically challenging, expensive, and time consuming. Yet, in order to mitigate hazards and prevent loss of life in these areas, and to better understand landslide processes, high-resolution measurements of landslide activity are necessary. Satellite-based synthetic aperture radar interferometry (InSAR) provides millimeter-scale measurements of ground surface deformation that can be used to identify and monitor landslides in remote areas where ground-based monitoring techniques are not feasible. Here we present a novel InSAR deformation detection approach, which uses double difference time-series with local and regional spatial filters and pixel clustering methods to identify and monitor slow-moving landslides without making a priori assumptions of the location of landslides. We apply our analysis to freely available Copernicus Sentinel-1 satellite data acquired between 2014 and 2017 centered on the Trishuli River drainage basin in Nepal. We found a minimum of 6 slow-moving landslides that all occur within the Ranimatta lithologic formation (phyllites, metasandstones, metabasics). These landslides have areas ranging from 0.39 to 1.66 km$^2$ and long-term dry-season displacement rates ranging from 2.1 to 8.8 cm/yr. Due to periods of low coherence during the monsoon season (June – September) each year, and following the 25 April 2015 $M_w$7.8 Gorkha earthquake, our time series analysis is limited to the 2014-2015 and 2016-2017 dry seasons (September - May). We found that each of the landslides displayed slightly higher rates during the 2014 period, likely as a result of higher cumulative rainfall that fell during the 2014 monsoon season. Although we do not have high quality InSAR data to show the landslide evolution directly following the Gorkha earthquake, the similar rates of movement before (2014-2015) and after (2016-2017) Gorkha suggest the earthquake had negligible long-term impact on these landslides. Our findings

highlight the potential for region-wide mapping of slow-moving landslides using freely available remote sensing data in remote areas such as Nepal and future work will benefit from expanding our methodology to other regions around the world.

# Introduction

Every year thousands of people are killed or impacted by landslide hazards (*Kirschbaum et al.*, 2015*, 2018*; *Froude and Petley, 2018*). Landslides not only cause harm to human life, but also cause disruption to day to day life and frequently inhibit the transport of goods and services, resulting in additional economic costs (*Oven, 2009*). Long-term records suggest that landslide hazards are increasing through time, with recent changes attributed to ongoing climate change and population growth (*Gariano and Guzzetti, 2016; Froude and Petley, 2018*). In addition to their hazardous impact, landslides dominate erosion and landscape evolution and also affect downstream aquatic habitat (*Kelsey, 1980; Larsen et al., 2010; Korup et al., 2010; May et al., 2013*). However, in most regions of the world, the characterization of landslide locations and impacts remain largely unknown due to the complex morphologies and geographic settings in which they typically occur and the difficulty of collating and updating inventories. Thus, in order to better understand how landslides may impact landscapes and communities, it is important that we continue to develop tools and techniques to identify and monitor these hazards.

Landslides can be mapped and monitored with field observations, digital elevation models, satellite and airborne imagery. However, because landslides are distributed over large areas, display a wide variety of behaviors, and occur under different climatic and geomorphologic regimes, no single observation strategy can be used to map and monitor all types of landslides. For instance, some landslides display slow creeping motion at meters per year or less in areas with high seasonal precipitation (e.g. *Hilley et al., 2004; Simoni et al., 2013*), while other landslides fail catastrophically and move downslope rapidly at rates of meters per second when triggered by earthquakes or storms (e.g. *Dahal and Hasegawa, 2008; Roback et al., 2018*). Remote sensing techniques are well suited for creating landslide inventories for a variety of mass movement types (e.g. *Nichol and Wong 2005; Kargel et al. 2016;Lacroix 2016*), while field-based mapping is better for detailed high quality measurements over small areas. Ideally, a data-fusion of both field-based mapping and remote sensing observations could be used to develop a complete landslide inventory, but this is often logistically challenging, time consuming, and expensive, especially in remote regions.

Interferometric synthetic aperture radar (InSAR) is a powerful tool used to study earth surface displacements over larger regions (up to 250 km wide swaths), and at a high spatial resolution (up to few meters). InSAR has been used frequently for studying earthquake cycle processes (e.g., *Bekaert et al., 2015c; Huang et al., 2016; Fielding et al., 2017*), volcanoes (e.g. *Amelung et al., 2000*), anthropogenic signals (e.g. *Jones et al., 2016; Buzzanga et al., 2020*), and landslides (e.g. *Colesanti et al., 2003; Hilley et al., 2004; Handwerger et al., 2013; 2019a; 2019b; Dai et al., 2019; Strozzi et al., 2018; Tantianuparp et al., 2013)*. Despite the wide applicability of InSAR to investigate a variety of geophysical phenomena, there are several challenges that often limit InSAR studies of landslides. Key challenges in using InSAR are related to decorrelation noise introduced due to radar scattering related landslide properties such as vegetation, deformation rate, and geometry, as well as superimposed spatially correlated noise signals introduced by propagation delays in the atmosphere (*e.g., Hanssen et al., 2001; Liang et al., 2018; Murray et al., 2019)*. Dense vegetation, which is common in landslide-prone regions with intense rainfall, is especially problematic and leads to increased noise that hinders InSAR monitoring of landslides. SAR sensors with longer radar wavelengths such as the L-band (24 cm radar wavelength) JAXA ALOS 1-2 satellites and the upcoming NASA-ISRO Synthetic Aperture Radar (NISAR) mission can penetrate vegetation and are better suited for monitoring landslides in vegetated areas. In addition, the ability to observe landslides using InSAR is limited by shadow and layover effects in steep terrain, due to the one dimensional viewing geometry of the radar sensor, which restricts displacement measurements to the radar look direction, and by the large changes in the ground surface from landslide deformation. It is possible to overcome some of these limitations by using SAR data from ground-based or airborne instruments. For instance, airborne instruments, such as the NASA/JPL UAVSAR, allow for targeted data collection that can be optimized for ground displacement sensitivity (Scheingross et al., 2013; Delbridge et al., 2016; Bekaert et al., 2019; Handwerger et al., 2019b). Although InSAR has been used for mapping and monitoring of landslides around the world , it is rarely applied to map landslides without prior knowledge of their location. However, with the availability of regularly acquired and freely available data, such as those from the Copernicus Sentinel-1 satellites, it is now possible to search for active landslide signals over entire mountain ranges (*e.g., Dehls et al., 2017*).

Here, we develop new InSAR analysis strategies to identify active slow-moving landslides in the steep mountainous terrain of Western Nepal. While recent studies (*Collins and Jibson, 2015; Kargel et al., 2015; Zekkos et al., 2017; Roback et al., 2018; Tsou et al., 2018*) have identified tens of thousands of landslides triggered by the April and May 2015 Gorkha earthquakes, there is also evidence of numerous slow-moving deep-seated landslides in the region that pre-date the earthquake (*Tsou et al., 2018*). We define slow-moving landslides as those having rates < 1.6 m/yr (*Hungr et al., 2014*). Despite these low rates, the hazardous and disruptive impact of these slow-moving landslides should not be neglected. Slow-moving landslides can display large displacements over periods of years (e.g., *Coe et al., 2009; Booth et al., 2018; Carrière et al., 2018; Nereson and Finnegan, 2018*) that can damage infrastructure such as roads, bridges, railways, dams, settlements, and pipelines (Merriam, 1960; *Mansour et* *al., 2011*). Because slow-moving landslides are difficult to detect without high resolution monitoring, it is common for communities to develop on or near the landslides (Geertsema et al. 2009; Mansour et al., 2011; Herrera et al., 2013; Dille et al., 2019). It is also common for faster-moving landslides to develop from within or immediately below the unstable ground associated with slow-moving landslides (*e.g., Reid et al. 2003*), and furthermore, slow-moving landslides have the potential to move rapidly or fail catastrophically due to rainfall or earthquakes (e.g., Carrière et al., 2018; *Guerriero et al. 2017; Handwerger et al., 2019a; Schulz and Wang, 2014*). Therefore one primary goal of this paper is to address the potential hazard of slow-moving landslides that are potentially impacting communities in the mountainous regions of Nepal.

In this manuscript, we use freely available InSAR data from the Copernicus Sentinel-1 satellites between 2014 and 2017 to identify and monitor slow-moving landslides in the Trishuli River catchment, Western Nepal. We develop a new methodology to identify landslides (and other localized deformation features) in challenging terrain with no prior knowledge of their location. We quantify the landslide metrics (area, length, width, slope, velocity) and explore relations between landslide activity and precipitation, and lithology. We also consider how these slow-moving landslides behave before and after the 2015 Gorkha earthquake.

# Study area

Our study area covers ~1230 km$^2$ in the Himalayas centered on the Trishuli River catchment (***Figure 1***). The elevation ranges from approximately 0.45 to 4.9 km with a mean elevation of approximately 2.2 km. The hillslope angle ranges from 0 to 65 degrees with a mean of 26 degrees (including valleys). The Trishuli River valley is V-shaped with steep inner gorges with a break in slope and more gentle slope angles moving towards the hilltops (***Figure S1***). The area is underlain by various lithologic units including the Galyang (slates, carbonates), Ghanpokhara (carbonaceous phyllites, slates, shales, limestones), Naudanda (quartzites), Ulleri (gneisses), and Ranimatta (phyllites, metasandstones, metabasics) formations (***Figure S2***; *Dhital, 2015*). The Main Central Thrust (MCT) runs through our field area and marks the transition between the Greater and Lesser Himalaya lithologic zones. Average annual rainfall between 2014 and 2018 was 1.4 m/yr (calculated from the Global Precipitation Measurement (GPM); *Huffman, 2017)* and occurs primarily during the monsoon season (June – September). Much of the area is vegetated, except for the locations that are terraced for agriculture, which are often those areas draped with landslide deposits. There is also a rapidly growing road network (*MacAdoo et al, 2018*), which predominantly consists of earthen roads, that traverse the valley walls connecting nearby villages .

The Himalayas are tectonically active due to the continental convergence between the Indian and Eurasian plates. The convergence rate is ~45 mm/yr with roughly 50% accommodated by the Main Himalayan Thrust (MHT) (*Lave and Avouac, 2000; Sella et al., 2002; Bilham, 2004*). The MHT has hosted a number of large earthquakes, the most recent of which was the $M_w$7.8 Gorkha event, which occurred on April 25, 2015 and ruptured a 140 km long section of the fault. This event was followed by a $M_w$ 7.2 aftershock on May 12, 2015. The total loss of life from these events was ~9000 people with an economic loss in billions of dollars (*Zhao, 2015*). The Gorkha earthquakes triggered a large number of landslides (*Collins and Jibson, 2015; Kargel et al., 2016*; *Martha et al., 2016; Zekkos et al., 2017; Roback et al., 2018; Tsou et al., 2018*). *Roback et al. (2018)* documented a minimum of 25,000 coseismic landslides, hundreds of which occurred in the Trishuli River catchment, and found that the highest density of landslides occurred in areas with relatively steeper slopes (mean slope angle 39 ± 9.1

degrees), higher annual precipitation, and that were proximal to the deepest sections of the fault rupture.

Our field area experienced significant shaking during the 2015 earthquakes. Peak ground acceleration during the $M_w$7.8 event was estimated at ~0.8g (Figure 1). Previous work along the Trishuli River catchment by *Tsou et al., (2018)* explored the role of topography and geology in controlling the landslides triggered by these earthquakes. Using digital elevation models, satellite and aerial photos, lithologic maps, and field work, *Tsou et al., (2018)* identified 912 coseismic landslides. They found that these landslides primarily occurred along the steeper V-shaped inner gorges underlain by gneiss and quartzite. They also identified 155 slow-moving, or dormant landslides along more gentle hillslopes located above the inner gorges (Figure S1). *Tsou et al. (2018)* refer to these landslides as "coherent landslides" and in the absence of any kinematic monitoring data, we refer to them as "potential slow-moving landslides". These landslides appeared mostly unaffected by the 2015 earthquakes, although many smaller yet catastrophic landslides were sourced from within these larger features (Figure S1).

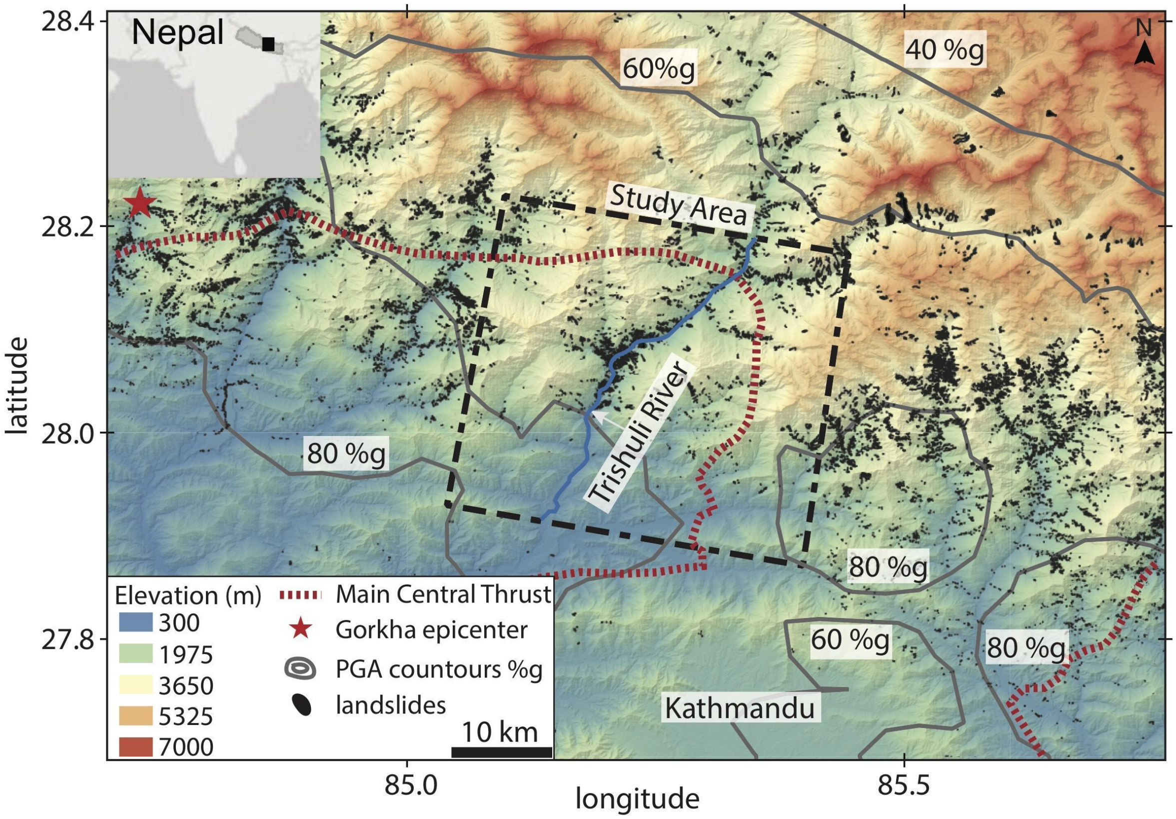


***Figure 1:*** *Elevation (meters above sea level) draped over a hillshade of the topography. Black dashed rectangle shows the study area along the Trishuli River. Blue line highlights the segment of the Trishuli River that lies within our field area. Dark gray contours show peak ground acceleration as a percentage of gravity (%g) for the Mw 7.8 Gorkha earthquake with red star showing epicenter. Black polygons show coseismic landslides mapped by Roback et al. (2018) and Tsou et al. (2018). Dotted red line shows the Main Central Thrust (MCT) fault. Elevation data from SRTM. Earthquake data from the USGS.*

180

# Data

For our study, we use Sentinel-1 C-band (5.6 cm radar wavelength) SAR data acquired between October 2014 and March 2017 by the European Space Agency under the European Commission Copernicus program. The Sentinel-1 constellation consists of two complementary satellites, one launched in March 2014 and one in April 2016, each having a 12-day repeat. Using data from both satellites provides a minimum 6-day repeat acquisition. All data are available free of charge from the Copernicus Open Access Hub (https://scihub.copernicus.eu/dhus/) and from the NASA Distributed Active Archive Center at the Alaska Satellite Facility (https://earthdata.nasa.gov/eosdis/daacs/asf). **Figure 2** shows the temporal distribution of Sentinel-1 acquisitions (black circles) between October 2014 and March 2017 in our study area (also summarized in **Table S2**). Data were collected with a 12 to 24 day repeat between October 2014 and September 2015, and a 6 to 12 day repeat between August 2016 and March 2017. Between September 2015 and August 2016 the repeat interval was reduced to ~1.5 months on average. We generated interferometric pairs spanning the three nearest acquisitions in time, while dropping interferograms that were too noisy to reveal any noticeable signal from the analysis. The lines shown in **Figure 2** represent the Sentinel-1 interferograms that we used in our Small Baseline time-series analysis, with the color representing the local average phase noise for each interferogram calculated as part of time-series analysis by removing spatially correlated noise sources and those correlated with perpendicular baseline in an iterative procedure (Hooper et al., 2012). The main sources of data noise in our study area is related to monsoonal precipitation, vegetation and snow, which causes decorrelation noise. The highest phase noise can be observed during the monsoon period (June-September), following the Gorkha earthquakes, and for those interferograms with longer temporal baselines. Given the high noise between June 2015 and August 2016, we are unable to recover the ground displacement time-series over our full study period. Therefore, we examine the data in the two periods with minimal noise, October 2014 to April 2015 and September 2016 to March 2017, which we refer to as the "pre-Gorkha" and "post-Gorkha" as they are separated by the April 2015 Gorkha Earthquake.

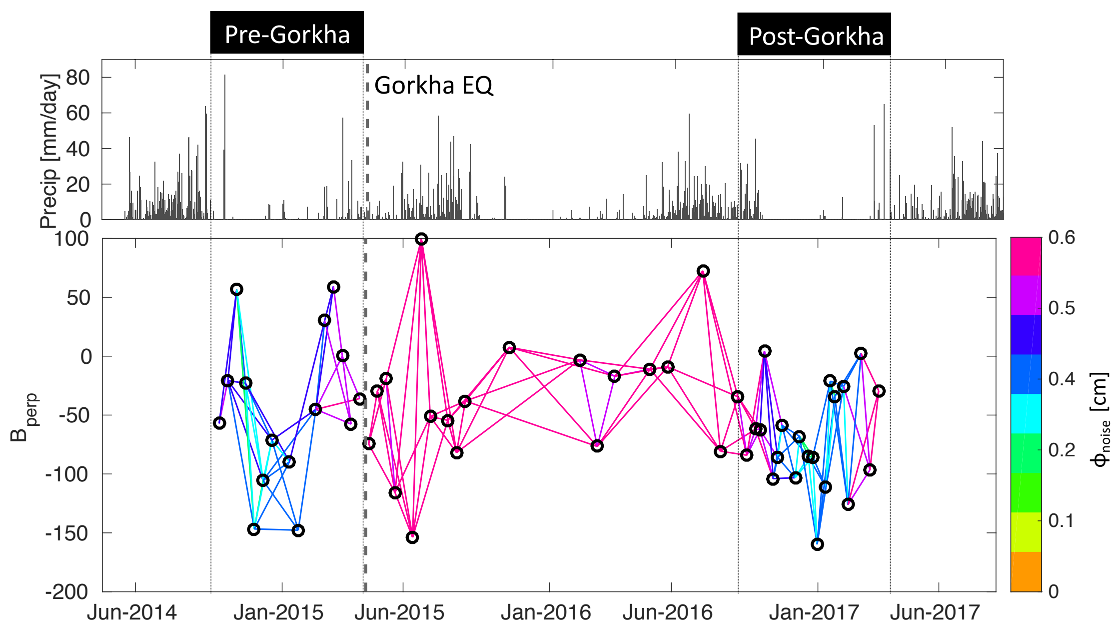


***Figure 2:*** *Perpendicular baseline plot of Sentinel-1 data (bottom panel) in the Trishuli River catchment, Nepal. Black circles represent individual SAR data acquisitions and lines show interferogram pairs with colors representing the average local phase noise for each interferogram as computed during time-series processing (Hooper et al., 2012). Higher phase noise can be observed in periods with sparse acquisition density immediately following the Gorkha earthquake and during the monsoon period. Daily precipitation total (average over our study area) is shown in the top panel from the Global Precipitation Measurement (GPM) mission (Huffman et al. 2017).*

# Methods

In this work we demonstrate a new methodology for analysis and detection of landslides using InSAR over a large region without prior knowledge of the location of landslides. Our methodological approach effectively handles the spatially-correlated longer-wavelength InSAR noise  (e.g., atmospheric and regional tectonic signals), which are typically superimposed over the InSAR data, by performing a spatial double difference time-series analysis (*e.g., Bekaert et al., 2019*). This methodology is also of value in the automation and operational monitoring of landslides and other geophysical phenomena with localized deformation patterns (i.e., sharp deformation gradient) using SAR data.

Our approach (summarized in supplemental Table S3)  consists of the following steps: first, we generate a stack of Sentinel-1 SAR images coregistered and resampled with respect to a master acquisition by using the Sentinel-1 stack processor (*Fattahi et al., 2017*) included in the InSAR Scientific Computer Environment (ISCE) (*Rosen, 2012*). Next, we perform a time-series analysis using the Small Baseline (SB) method in StaMPS (*Hooper et al., 2012*), leveraging the ISCE to StaMPS capability in ISCE to ingest our Sentinel-1 coregistered stack (*Bekaert et al., 2017*), to down-select pixels, and improve the signal to noise ratio in the data. Other approaches such as Persistent Scatterer (e.g., Ferretti et al., 2001; Hooper et al., 2004), SqueeSAR (e.g. Ferretti et al., 2011), and the Sequential Estimator (e.g., Ansari et al., 2017) could be leveraged as well for pre-processing and to down-select pixels. The unwrapping of the interferograms is not a trivial step. To focus our analysis, we mask out pixels over flat terrain (slope < 5 degrees), as these are unlikely to contain landslides, and additionally remove  as well as pixels that are in shadow or lay-over (e.g., Hanssen 2001), as the signal in such pixels is a superposition of the signal coming from multiple distinct geographical locations . We leverage StaMPS' iterative phase closure approach (Hussain et al., 2016) and its 3D unwrapping capabilities (Hooper et al., 2012) followed by a visual inspection of the interferograms to limit phase unwrapping errors. While down-selecting pixels during time-series processing improves the signal to noise ratio, it does not address the issue of spatially correlated noise-sources superimposed on landslide signatures, such as those originating from tectonic processes (*e.g., Ader et al., 2012*) and atmospheric propagation delays due to the ionosphere (*e.g., Liang et al., 2018*) and troposphere (*e.g., Hanssen 2001; Bekaert et al., 2015a*). Different strategies can be used to reduce these superimposed noise-terms including the application tropospheric mitigation tools *(e.g., Jolivet et al., 2011; Bekaert et al., 2015b),* ionospheric correction estimated from the data (*e.g., Liang et al., 2018; Liao et al., 2018*), and correcting for tectonic noise using a forward model (*e.g., Bekaert et al., 2018*). However, these model based corrections can introduce additional noise in the data. For example, tropospheric corrections from weather models are likely to introduce turbulent noise (e.g., Hanssen 2001), while the assumption of a phase-based linear correction might not hold over large regions with complex topography as mountains could be blocking weather dynamics (e.g. Bekaert et al., 2015a). Existing time-series packages often leverage a spatial and temporal filter to reduce contamination of atmospheric noise or simply apply a low pass filter to remove any longer-wavelength signals (e.g., Hooper et al., 2004). As InSAR is a relative measurement, all pixels are moving with respect to a pre-defined spatial reference point. The selection of this reference point is not trivial, as the above mentioned noise sources can make it challenging to select a stable reference area for InSAR because uncertainty due to atmospheric noise increases with distance from the reference area. Additionally, these noise sources can make it challenging to identify meaningful landslide signatures over large regions from an individual average velocity map (Figure 3A). A more direct approach for investigating localized deformation patterns is to apply a double difference method between two closely located pixels, which cancels out spatially correlated signals at distances exceeding the separation between these pixels. Such an approach is regularly applied as a post-processing step to show and visualize how a feature, such as a landslide (*e.g., Dille et al,. 2019; Handwerger et al., 2019a; 2019b*) or critical infrastructure (*e.g., Bekaert et al., 2018*), is deforming compared to its surrounding stable area (i.e. a local reference point), but is rarely applied as part of the processing of the time-series itself to reveal localized signals in the first place.

We implemented the double differencing approach as part of our time-series processing workflow over the full study area. First, we spatially filter each interferogram by differencing the output of a regional and local averaging filter kernel, where we use a smaller radius for the local kernel compared to the regional kernel. By differencing both kernels, we have defined the regional pixels (whose extent is fixed by the regional kernel) to act as the reference area for the local pixels. Both the regional and local kernels could also be combined into a single more complex filter, but for illustrative reasons and simplicity we kept them separate. Second, we apply conventional time-series analysis in which we estimate an average linear velocity map from these filtered interferograms (***Figure 3B***) with corresponding uncertainties estimated from bootstrapping the InSAR time-series (Figure 3C) . Given that the filtering step is applied to the complete image, the result reveals regions with a strong localized signal will have a positive and negative alternation in the estimated rate (e.g., see location A in ***Figure 3B***). One of the key items for investigation is the sensitivity of the kernel size of the filters as well as the shape of the kernels. The larger the averaging kernel, the more sensitive our analysis becomes to the longer-wavelength processes and thus leads to an increased uncertainty in the time-series. We tested various combinations of filter sizes including varying the local kernel from 100 m to 200 m, and the regional filter from 1 km to 2 km. For the local kernel we fixed its shape to be a disk and for the regional filter we used a disk- and a donut-shaped kernel but did not find noticeable differences in identifying hotspots of localized deformation using these different shapes (see ***Figure S4***).

We use this double-difference filtering approach to identify slow-moving landslides that are moving during our study period. Active slow-moving landslides tend to display episodic or continuous downslope motion, which can be approximated as a linear trend in time, with short term or seasonal variations in velocity driven by changes in stress conditions (e.g., rainfall and snowmelt)  (Merriam 1960; *Handwerger et al., 2013; 2019a;b*; *Cohen-waeber et al., 2018; Dille et al., 2019*). Both the rate and uncertainty are considered together when assessing whether a certain localized deformation feature is moving with confidence. We therefore derive another mask with only pixels that experience a significant rate, where the magnitude of the rate over the observation period $|v|$ needs to be at least two times larger than the uncertainty of the rate $\sigma_v$ (i.e. $|\Delta V_{LOS}| - 2\sigma_{\Delta V_{LOS}}$>0). We note that pixels for which the displacement history is nonlinear in time have a larger uncertainty. Thus, our method is best-suited for identifying landslides that are active during the full study period and that are less impacted by seasonal effects. Finally, we apply a clustering algorithm that requires a minimum of 3 pixels per cluster to reveal larger localized features and help reduce noise (***Figure 3D***). The mask of significant rates allows us to rapidly narrow down the regions that would benefit from a closer inspection (i.e., landslides).

To identify active landslides from the clusters shown in Figure 3D, we manually examined the clusters to find those with the highest velocity (i.e. largest signal to noise ratio) and largest spatial signal, which we could confidently identify as landslides. It is possible that some of the clusters removed from our analysis (and possibly some of the pixels removed before clustering) may correspond to active landslides (i.e., true positives). However, these removed clusters are small in spatial scale and have small displacement magnitudes that are close to our detection limit. Similarly, some clusters just meeting our detection threshold are likely a mixture of small landslides and leakage of high-frequency tropospheric noise that varies over spatial scales of a few 100's of meters. After we selected the active landslides, we used a 10 meter digital elevation model (DEM) made available by the NASA High Mountain Asia project (*Shean et al., 2016; 2017*), blending DEMs derived from high-resolution WorldView imagery (<1 m) with that of the ASTER (30 m), and Google Earth images to map the boundaries and measure the geometry (area, length, width, mean slope angle) of each landslide (***Figure 4***; ***Table S1***). We also compared the landslide motion and InSAR data quality to rainfall data from the Global Precipitation Measurement (*Huffman, 2017)*.

313

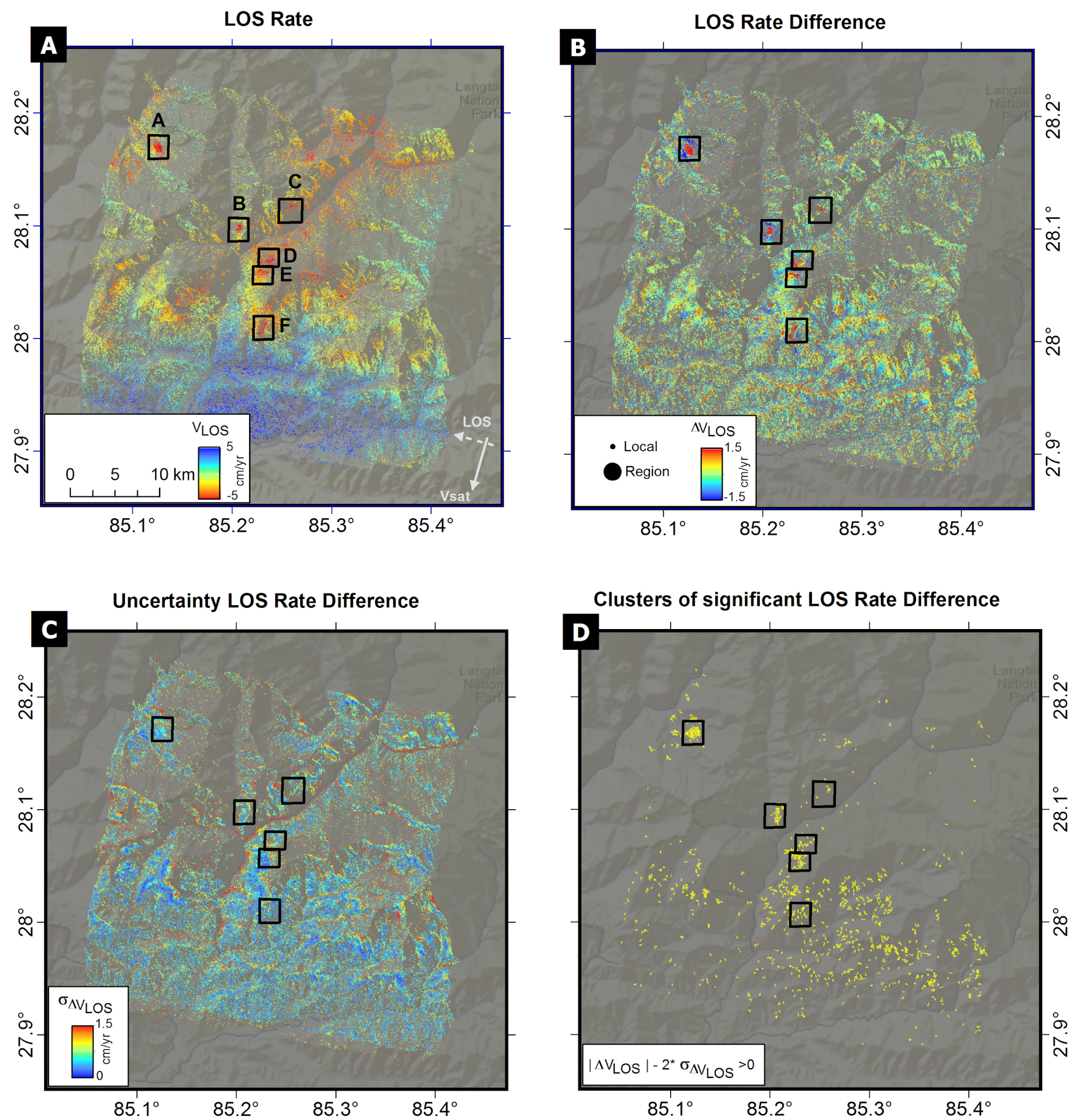


***Figure 3:*** *InSAR landslide analysis for pre-Gorkha period between October 2014 and April 2015. For post-Gorkha period see* ***Figure S3****. (A) Average line-of-sight (LOS) rate map over the period of observation. The image contains various signals including tectonic deformation, atmospheric noise, and local deformation signals due to human impact and landslides. (B) LOS rate map after applying double difference method. Our double difference method using a*

*local and regional detector kernels reveals localized deformation signals ($\Delta V_{LOS}$) cancelling out the long wavelength tectonics and atmospheric noise signals. The filter size as shown in the legend is drawn to scale. (C) Corresponding local rate uncertainties ($\sigma_{\Delta V_{LOS}}$) estimated from bootstrapping the time-series of local deformation. (D) Yellow pixels show significant local rates ($|\Delta V_{LOS}| - 2\sigma_{\Delta V_{LOS}}$>0) with a minimum 3-pixel cluster filter applied. Key clusters (i.e. landslides) A-F are highlighted by the black boxes . Variation of the filter size and shape does not impact the identified significant clusters (**Figure S4**).*

# Results

The quality of the Sentinel-1 InSAR data varies significantly over the 2.5 year study period. InSAR analysis in steep and mountainous regions, like Nepal, are often plagued by noise due to precipitation, vegetation, and atmospheric effects, and from large surface changes due to slope deformation. We find there is a large increase in phase noise in the time-series between June 2015 and August 2016 (**Figure 2**), which is likely a result of vegetation growth and changes in the ground surface properties during the monsoon (June-September) and from the Gorkha earthquake. In addition, the relatively infrequent Sentinel-1 revisit time between September 2015 and August 2016 further restricts our ability to recover the ground displacement time-series during our study period. As described in the Methods section above, we therefore perform our landslide analysis by comparing October 2014 to April 2015 (labeled “pre-Gorkha”) and September 2016 to March 2017 (labeled “post-Gorkha”).

Our clustering approach reveals multiple regions to have significant local displacement rates (**Figure 4D**) both prior to and after the 2015 earthquakes. In our analysis we focused our attention on those clusters that have the highest local displacement rates (**Figure 4B**). We identified 6 slow-moving landslides that are moving during both the pre-Gorkha period (***Figure 4***) and post-Gorkha period (***Figure S3***). The landslides are large features with lengths ranging from 490 to 2748 m, widths from 605 to 795 m, areas from 0.39 to 1.66 $km^2$, and mean slope angles from 17 to 28° (summarized in ***Table S1***). Each landslide occurs within the Ranimatta Formation, which is composed of phyllites, metasandstones, metabasics (***Figure S2***). Our displacement time series shows that each landslide exhibits slow but apparently near-continuous average rates of motion (***Figure 5***). Although we have no high-quality InSAR data during the monsoon season, we assume that the landslide motion is in part driven by intense and sustained precipitation that falls during that time period and infiltrates into the landslide body and increases the pore-water pressure. Our study site received ~1.3 m of rainfall between June-October 2014 and ~1.1 m of rainfall between June-October 2016. We fit linear functions to the displacement time series to characterize the dry season landslide velocity between October 2014 - April 2015 and October 2016 - April 2017. The LOS displacement rate ranges from -88 mm/yr to -21 mm/yr, with a negative value referring to ground surface motion away from the radar. All of the landslides were moving faster during 2014 - 2015 time period than the 2016 - 2017 time period. The increased velocities in 2014 likely result from the increased rainfall during the 2014 monsoon when compared to 2016.

As described above, we performed our InSAR analysis without prior knowledge of active landslides in the Trishuli River catchment. Our goal was to develop a methodology that could be applied to areas with no landslide inventory. Once we mapped the active landslides, we compared our results to a previously published landslide inventory from *Tsou et al. (2018)* *(**Figure 4**)* to provide an independent check on our ability to detect landsliding. *Tsou et al.*

*(2018)* mapped landslides using stereo-pair aerial photos and field validation. They identified landslides by mapping deformation features such as scarps or ground offsets. We find that landslides B-F lie within previously mapped “coherent” or potentially slow-moving landslide boundaries (***Figure 4***), which provides additional evidence that we have identified landslides. Our InSAR analysis also reveals that many of the other previously mapped landslides contain some minor deformation signals (i.e. high LOS velocity; ***Figure 4***). However, we do not map these as active landslides because these features did not meet our landslide detection criteria (described in Methods) and we believe that further investigation is required to determine their state of activity.

Our field site experienced significant ground accelerations (up to 80% g according to the USGS ShakeMap) during the 2015 Gorkha earthquake (**Figure 1**), yet landslides A-F were not significantly impacted in that they did not fail catastrophically and displayed relatively similar velocities during the pre-Gorkha and post-Gorkha periods. It is possible (and likely) that the landslides displayed a period of accelerated slip immediately following the earthquakes, which has been observed in other settings (*Lacroix et al., 2014; 2015; Bontemps et al., 2020*); however, we are unable to reliably measure surface displacements for 2.5 years following the Gorkha earthquake.

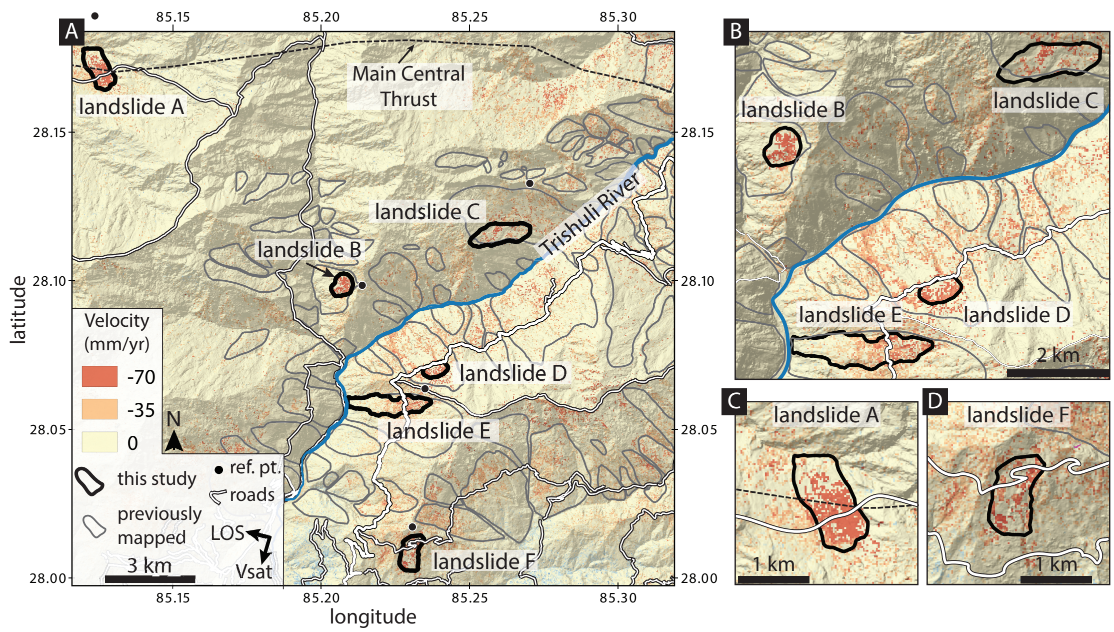


***Figure 4.*** *Landslide inventory map and InSAR line-of-sight (LOS) velocity for the pre-Gorkha period (October 2014-April 2015) draped over a hillshade of the topography. Regional scale inventory shown in panel (A) and close up view of landslides shown in panels (B-D). A velocity value of 0 corresponds to pixels that have been masked out but is set to yellow color for viewing purposes. Black polygons show the landslides identified using our InSAR methodology. Gray polygons show potentially slow or "coherent" landslides mapped by Tsou et al. (2018). Black circles show the local stable reference point for each landslide as used for generating the time-series histories in Figure 5. . Note that the stable reference point for landslide A lies just outside the clipped frame. Black dashed line shows the Main Central Thrust. Black arrows show the satellite LOS and flight direction (Vsat). Blue line corresponds to the Trishuli river and white lines show the road network.*

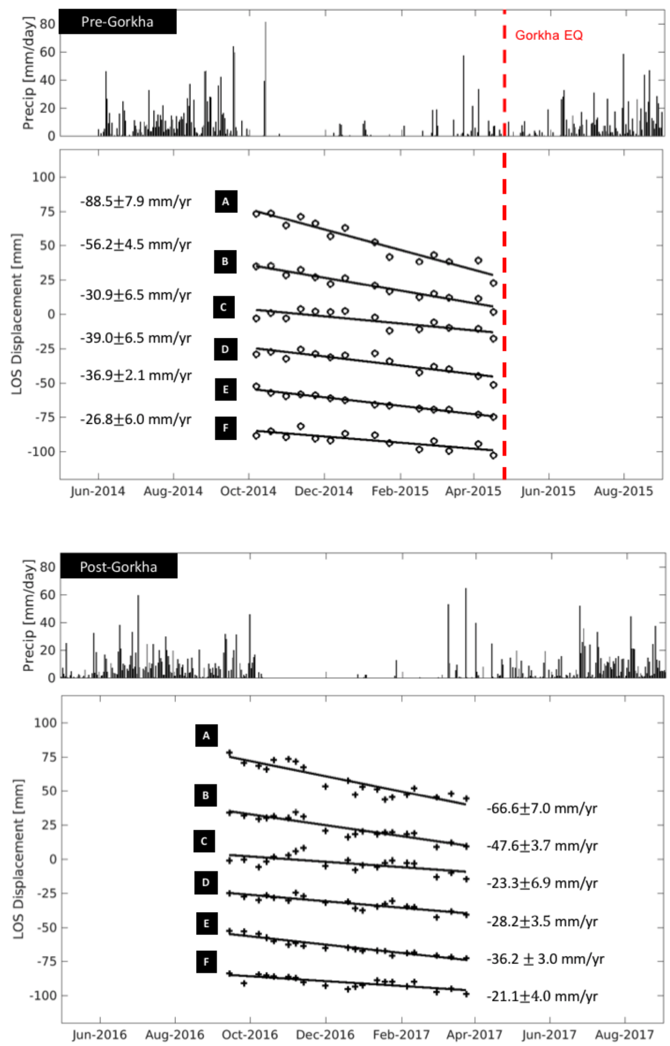


***Figure 5:*** *Line-of-Sight (LOS) displacement history for landslides A-F with respect to their local stable reference (black circle marker in* ***Figure 4)****, for pre-Gorkha (top) and post-Gorkha (bottom) periods. Displacement histories for each landslide are offset arbitrarily on the y-axis for visualization purposes, and thus do not allow for absolute comparison between them. However, the rate at which displacements vary in time can be compared. A radius of 250 m is used for averaging both the reference point and landslide center. Daily precipitation for the pre-Gorkha and post-Gorkha time periods are shown in the top and bottom panel, respectively. The Gorkha earthquake event is indicated by the red line in the*

*top-axis. Reported rate uncertainty corresponds to 1-sigma.* 2D cumulative displacement time-series for each landslide are included as supplemental Figure S6-S7 for respectively the before and aftter Gorkha periods.

# Discussion

The Trishuli River catchment is well known for its landslide activity, however, most recent research has focused on catastrophic landslides triggered by the 2015 earthquakes (e.g., *Roback et al., 2018; Tsou et al., 2018*). Slow-moving landslides in Nepal also pose a major hazard (*Caine and Mool, 1982; Mansour et al. 2011; Tsou et al., 2018*) because they 1) can remain active for many years or decades and thus can accumulate large deformations (e.g., *Coe et al., 2009; Nereson and Finnegan, 2018*), 2) can display "surges" or short periods of rapid motion at relatively high rates ($10^2$-$10^3$ m/yr) (e.g., *Hungr et al., 2014; Guerriero et al. 2017; Carrière et al., 2018*), and 3) have the potential to fail catastrophically (e.g., *Handwerger et al., 2019a; Inrieri et al., 2018; Kilburn and Petley, 2003*). The resulting displacements can damage infrastructure such as roads, bridges, railways, dams, settlements, and pipelines. Given that landslides A and D-F cut across the road network (**Figure 4**), and are moving at rates between ~20-90 mm/yr, (**Figure 5**), using the scale proposed by *Mansour et al. (2011),* these landslides will or have likely already caused moderate damage and disruption to the road network. . In addition, many of the slow-moving landslides, given their loose and relatively easily tillable nature, are terraced for agriculture (**Figure 4**), which leads people to develop, and even live on their surfaces. Furthermore, damaging and potentially life threatening fast-moving landslides, such as debris flows, can initiate from within the disrupted mass of active slow-moving landslide body (e.g., *Reid et al., 2003; Booth et al., 2018*), suggesting a need for these areas to be identified as part of a geohazards assessment. Following the Gorkha earthquake, *Tsou et al. (2018)* found that 912 earthquake-induced landslides were triggered along the steep (slope angle > 35 deg) inner gorges of the Trishuli River. They also found that the "coherent" (i.e., slow-moving or dormant) landslides exhibited no obvious signs of reactivation by the earthquakes, however, many of the rapid landslides in their inventory initiated from within larger coherent landslide bodies. We note that from our inventory, only landslide B and landslide E contain mapped rapid landslides (Figure S1) from the Gorkha earthquake (Tsou et al., 2018). However, our main findings show that the active slow-moving landslides along the Trishuli River occur on the more gentle slopes (slope angle ~ 22 deg) above the steep inner gorges and are thus less likely to be subject to rapid catastrophic failures

Due to data limitations (i.e., low coherence) following the earthquakes, we were unable to analyze the coseismic or immediate post-seismic deformation of landslides A-F. However, our findings suggest that these landslides were not accelerated, and rather were perhaps decelerated by the 2015 earthquakes. Yet, given that strong ground motion occurred along the Trishuli River (**Figure 1**), these landslides may have accelerated for a short time period following the earthquakes or in the subsequent monsoon season that started approximately three weeks after the earthquakes. Similar landslide behaviors have been observed at the Maca landslide in Peru, where slow-moving landslides accelerated in response to a $M_w$ 6.0 earthquake and then decelerated back to its pre-earthquake rates over the following 35 days (*Lacroix et al., 2014; Bontemps et al., 2020*). These behaviors suggest that the rate-strengthening frictional mechanisms may inhibit runaway acceleration of these landslides (*Wang et al., 2010; Lacroix et* *al., 2014; Handwerger et al., 2016; Agliardi et al., 2020*). Despite no significant acceleration impact from the recent major earthquakes, strong ground motion may influence the long term stability and evolution of these landslides (Bontemps et al,. 2020).

The data volume from SAR has grown rapidly with the launch of Sentinel-1, and will further expand with observations made from the Canadian Radarsat Constellation Mission (RCM) and in future the NISAR mission. The regular acquisition repeat interval and global mapping of these new sensors enables the use of time-series InSAR for long-term monitoring of landslides. Specifically, the European Commision has committed to operate the Sentinel-1 constellation until at least 2030, which will enable monitoring of hillslopes from weeks to decades. Our developed methodology approach allows wide area mapping of slow-moving landslides without prior assumption where landslides occur. This also allows for ongoing monitoring of slopes and for a rapid expansion of slow-moving landslides in existing inventories. By increasing the number of observations of slow-moving landslides in catalogues, a larger statistical dataset will be available to investigate the correlation with physical drivers such as precipitation and snowmelt, which will allow for an improved understanding of the mechanisms that control these types of landslides.

# Conclusions

In this study, we investigated hillslope deformation along the Trishuli River catchment in Nepal, where hundreds of coseismic landslides were triggered during the 25 April 2015 $M_w$7.8 Gorkha earthquake. We used time-series InSAR from the Copernicus Sentinel-1 satellites to identify active landslides. We presented a novel method for the detection of landslides (and other localized deformation) over a large region without prior assumptions of the geographical location of any landslide. Our method consists of a local double difference approach, implemented through a filtering step that is applied to the individual interferograms prior to time-series estimation. Our approach effectively cancels out long-wavelength noise processes (e.g., tectonic processes, ionospheric and tropospheric noise) and reveals localized deformation patterns. We further narrow down the search for landslides by examining clusters of neighboring pixels that exhibit significant displacement rates, here defined as rates twice the uncertainty. Our new approach allowed us to identify a minimum of 6 large, slow-moving landslides within our study area where continuous deformation is likely driven by monsoonal precipitation. Most of these landslides are proximal to roads and infrastructure and thus will likely cause damage and disruption that will impact the local communities.

While we were unable to examine the immediate response of these landslides to the 2015 Gorkha earthquake, we found that their deformation rates before and 2.5 years after the earthquake were similar, which suggests that, despite experiencing significant ground accelerations, these landslides were largely unaffected by the earthquake over annual timescales. One of the main advantages of our InSAR-based approach is that it provides an opportunity to monitor ground surface deformation in remote areas. An area of future research is to couple the Sentinel-1 data with additional data acquisitions from other SAR sensors such as Cosmo-SkyMed, RadarSat Constellation Mission, ALOS-2, and NISAR. Combining data from multiple satellites with different radar wavelengths may provide further insight into the complex dynamics of landslides. We will also seek to test this method elsewhere (such as the Western

United States) where the morphologies, failure modes, and orientation of landslides may highlight additional opportunities and challenges using our methodology.

# Acknowledgements

This research was carried out at the Jet Propulsion Laboratory, California Institute of Technology, under a contract with the National Aeronautics and Space Administration. Part of ALH's research was supported by an appointment to the NASA Postdoctoral Program at the Jet Propulsion Laboratory, administered by Universities Space Research Association under contract with NASA. DPSB and DBK's research was supposed by NASA's High Mountain Asia Program (NNH15ZDA001N) under grant NNX16AT79G. The Copernicus Sentinel-1 SAR data used in our study was processed up to SLC level by ESA, and downloaded from the ASF DAAC (https://earthdata.nasa.gov/eosdis/daacs/asf). The daily accumulated precipitation (final run) data were provided by the NASA/Goddard Space Flight Center's and PPS, which develop and compute the GPM_3IMERGDF.05 dataset as a contribution to GPM, and archived at the NASA GES DISC (*Huffman 2017*). Shakemap and earthquake information was provided by the USGS (https://earthquake.usgs.gov/earthquakes/). We thank the NASA High Mountain Asia project (*Shean et al., 2016, 2017*) for providing us with a 10 meter digital elevation model (DEM) used for landslide mapping and computing landslide statistics, and also thank the Jet Propulsion Laboratory for providing us with ISCE (*Rosen et al., 2012*), the stack processing capability (*Fattahi et al., 2017*), and the SRTM topographic data (*Farr et al., 2007*). We also greatly acknowledge Nick Rosser, Tom Robins and Jack Williams, at Durham University (UK), for providing us with on-the-ground photos and expert guidance on interpreting and corroborating the mechanisms impacting landslides in the study area based on their field work and knowledge of the study area. We thank John Elliot for providing a shapefile of the Main Central Thrust fault. Part of the figures were prepared using ARCGIS and QGIS. We acknowledge Google Earth, Esri, HERE, Garmin, OpenStreetMap contributors, the GIS user community, QGIS

Geographic Information System, and the Open Source Geospatial Foundation Project (http://qgis.osgeo.org).

# Supplemental figures:

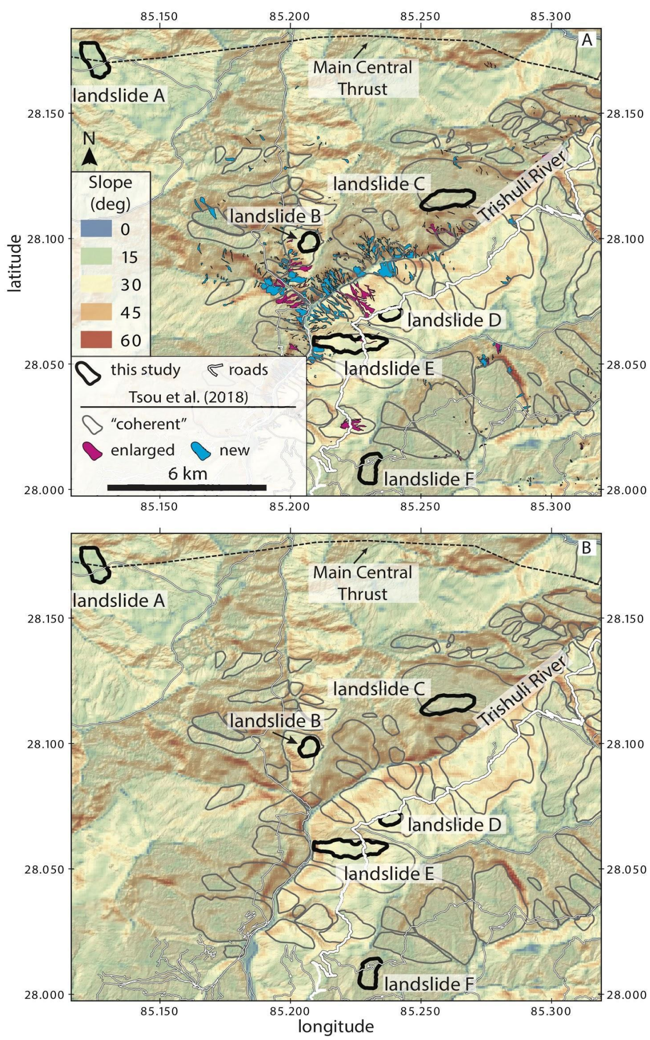


***Figure S1:*** *Topographic slope map and landslide inventory in the Trishuli Valley. Panel A shows the landslide polygons for catastrophic landslides (blue and magenta) triggered by the Gorkha earthquake sequence and the "coherent" landslides mapped by Tsou et al., (2018).*

*Panel B shows the slope map with the catastrophic landslide inventory removed for clarity Most catastrophic landslides occurred along the steep inner gorges. We find the deep-seated landslides to occur on the intermediate slopes between 16.5° and 27.5°.*

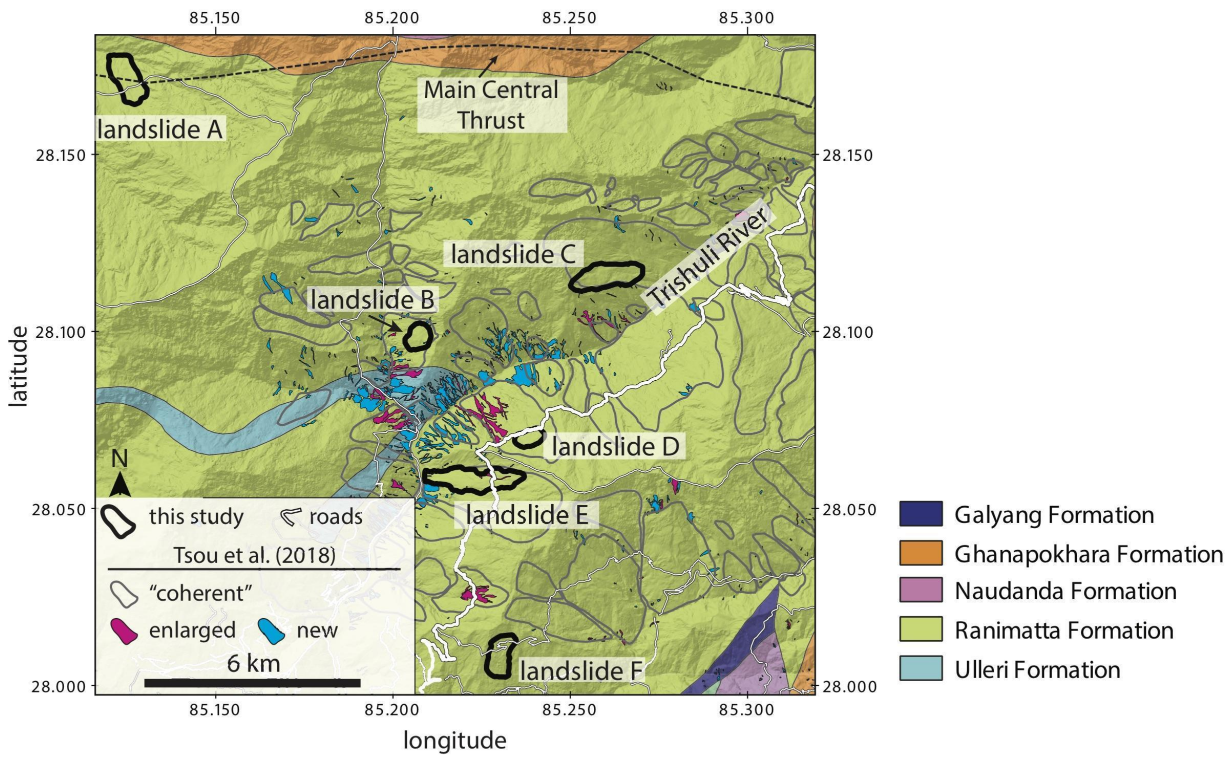


***Figure S2:*** *Lithologic map for section the Trishuli River catchment shows units of Galyang (slates, carbonates), Ghanpokhara (carbonaceous phyllites, slates, shales, limestones), Naudanda (quartzites), Ulleri (gneisses), and Ranimatta (phyllites, metasandstones, metabasics) formations (Dhital, 2015). Landslide polygons for catastrophic landslides (blue and magenta) triggered by the Gorkha earthquake sequence and the "coherent" landslides mapped by Tsou et al., (2018).*

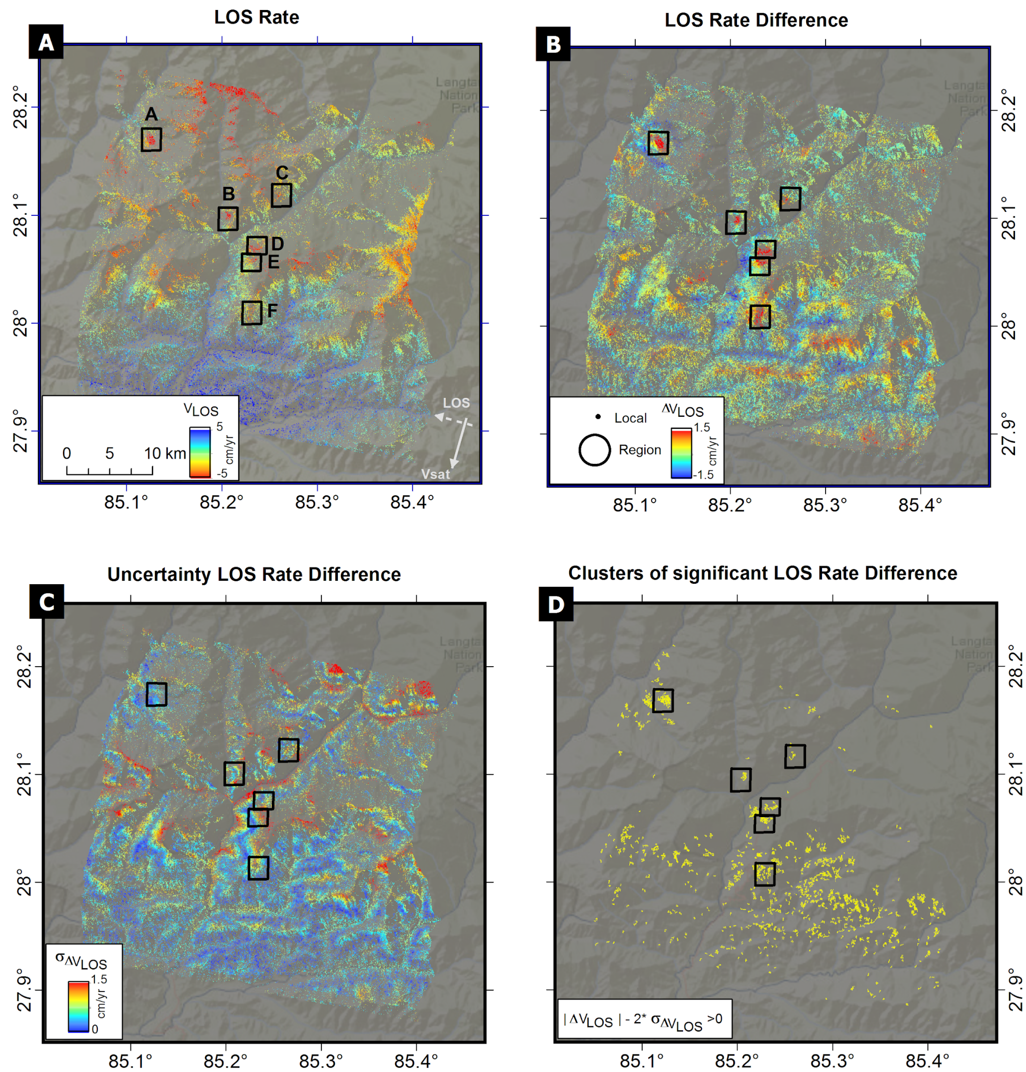


***Figure S3:*** *InSAR landslide analysis for post-*Gorkha *period between September 2016 and May 2017. For pre-Gorkha period see* ***Figure 3****. (A) Average line-of-sight (LOS) rate map over the period of observation. The image contains various signals including tectonic deformation, atmospheric noise, and local deformation signals due to human impact and landslides. (B) LOS rate map after applying double difference method. Our double difference method using a local and regional detector kernels reveals localized deformation signals ($\Delta V_{LOS}$) cancelling out the long wavelength tectonics and atmospheric noise signals. The filter* *size as shown in the legend is drawn to scale. (C) Corresponding local rate uncertainties ($\sigma_{\Delta V_{LOS}}$) estimated from bootstrapping the time-series of local deformation. (D) Yellow pixels show significant local rates ($\left|\Delta V_{LOS}\right| - 2\sigma_{\Delta V_{LOS}}$>0) with a minimum 3-pixel cluster . Key clusters (i.e. landslides) A-F are highlighted by the black polygons.*

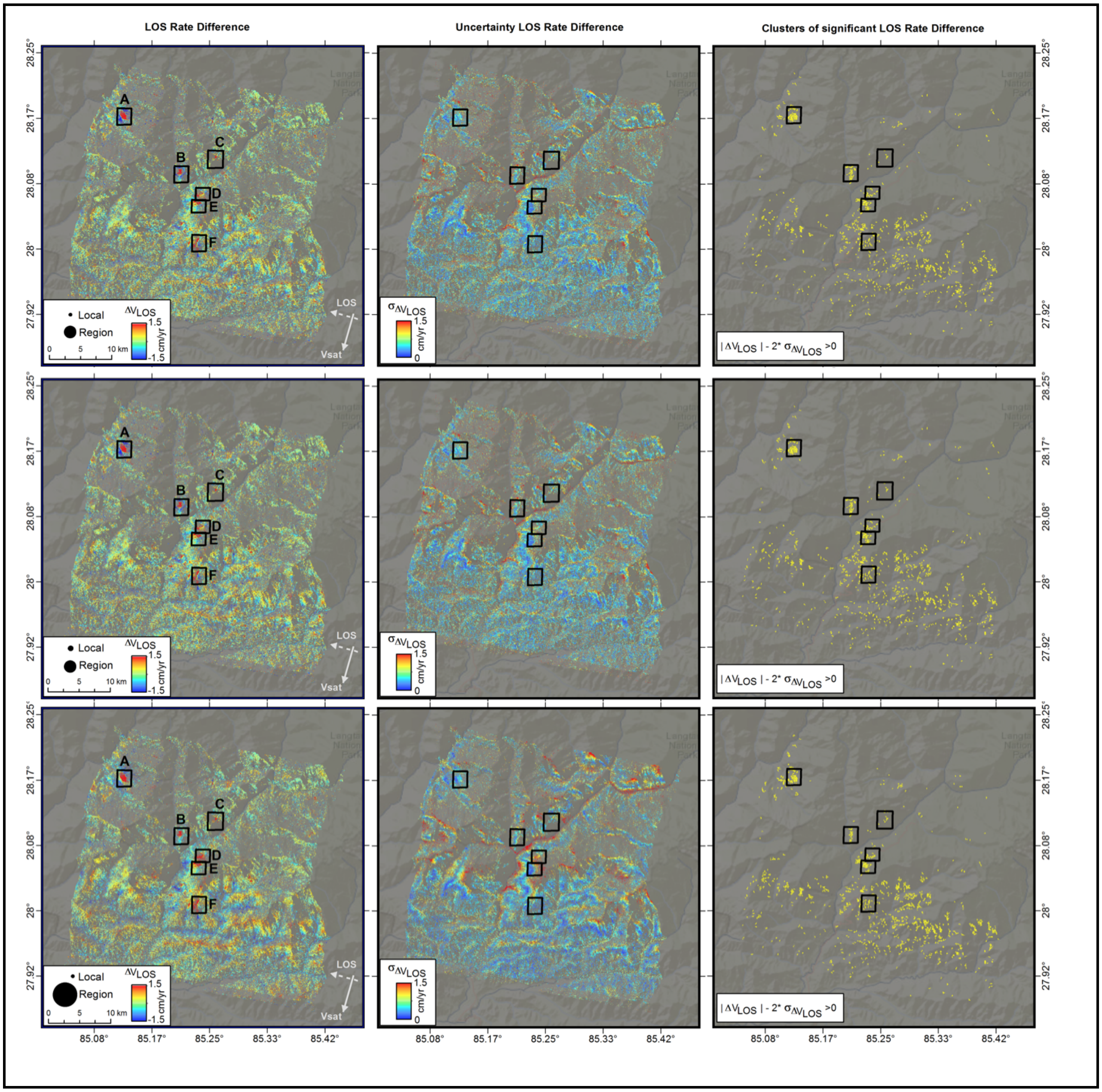
LOS Rate Difference
Uncertainty LOS Rate Difference
Clusters of significant LOS Rate Difference
A
B
C
D
E
F
Local
Region
ΔV LOS
1.5
-1.5
cm/yr
0
5
10 km
LOS
Vsat
σ ΔV LOS
0
|ΔV LOS| - 2* σ ΔV LOS >0
28.25°
28.17°
28.08°
28°
27.92°
85.08°
85.17°
85.25°
85.33°
85.42°

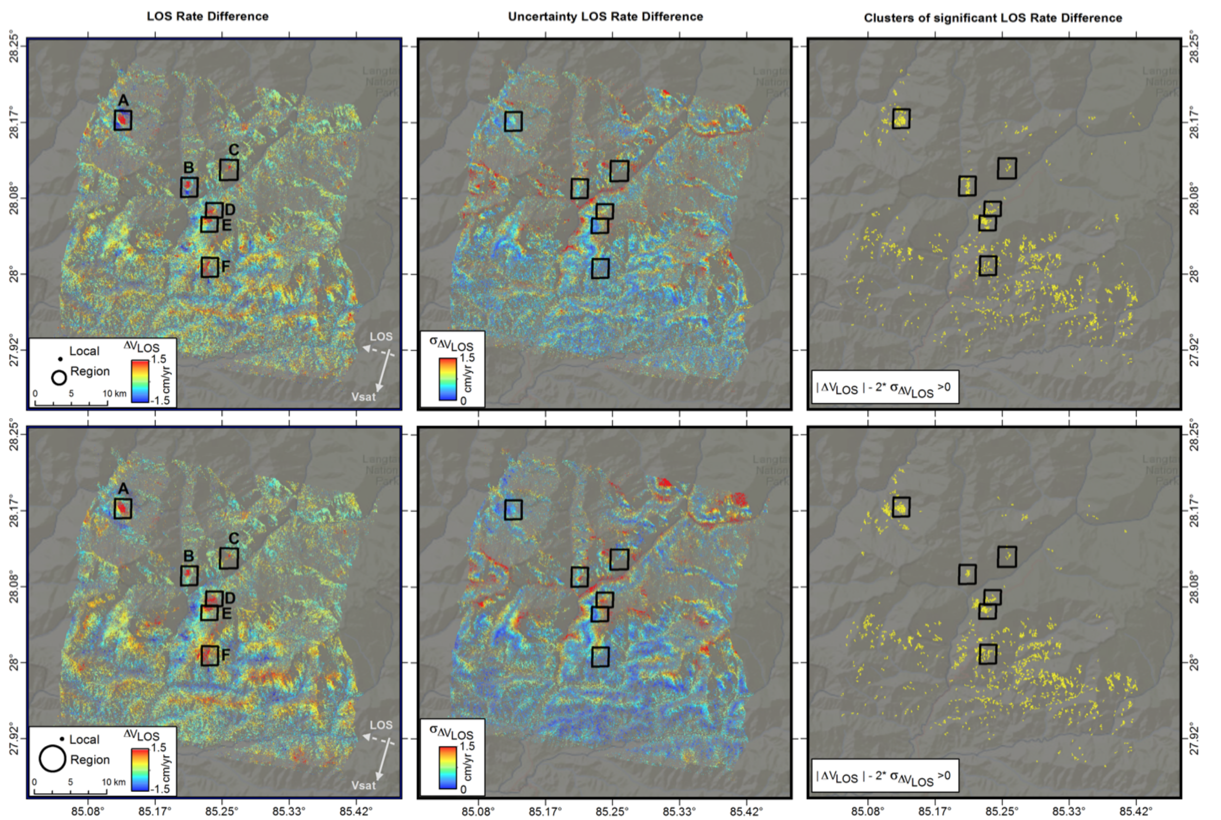


***Figure S4:*** *Sensitivity analysis for filter kernel size and shape for the pre-Gorkha period (October 2014 and April 2015). Each row shows the analysis for a different kernel filter as shown in the legend. The filter size as shown in the legend is drawn to scale. First column shows the line-of-sight (LOS) rate estimated filtered with local and regional kernel filter to reveal localized rate signals ($\Delta V_{LOS}$). Second column shows the local rate uncertainties ($\sigma_{\Delta V_{LOS}}$) estimated from bootstrapping the spatially filtered time-series. Third column shows the significant local rates ($|\Delta V_{LOS}| - 2\sigma_{\Delta V_{LOS}} > 0$) with a minimum 3-pixel clusters. Changes in the filter kernel size and shape does not appear to have a strong impact on the identified clusters. Key clusters (i.e. landslides) A-F are highlighted by the black polygons.*


***Figure S5:*** *Field photos of landslides C, D, and E (see* ***Figure 4*** *for location). Photos of landslide E are provided from two perspectives. The photos provide a ground based view of the landslides and show agriculture and ground surface deformation that is impacting the Trishuli highway (Photos courtesy of Jack G. Williams, Durham University).*

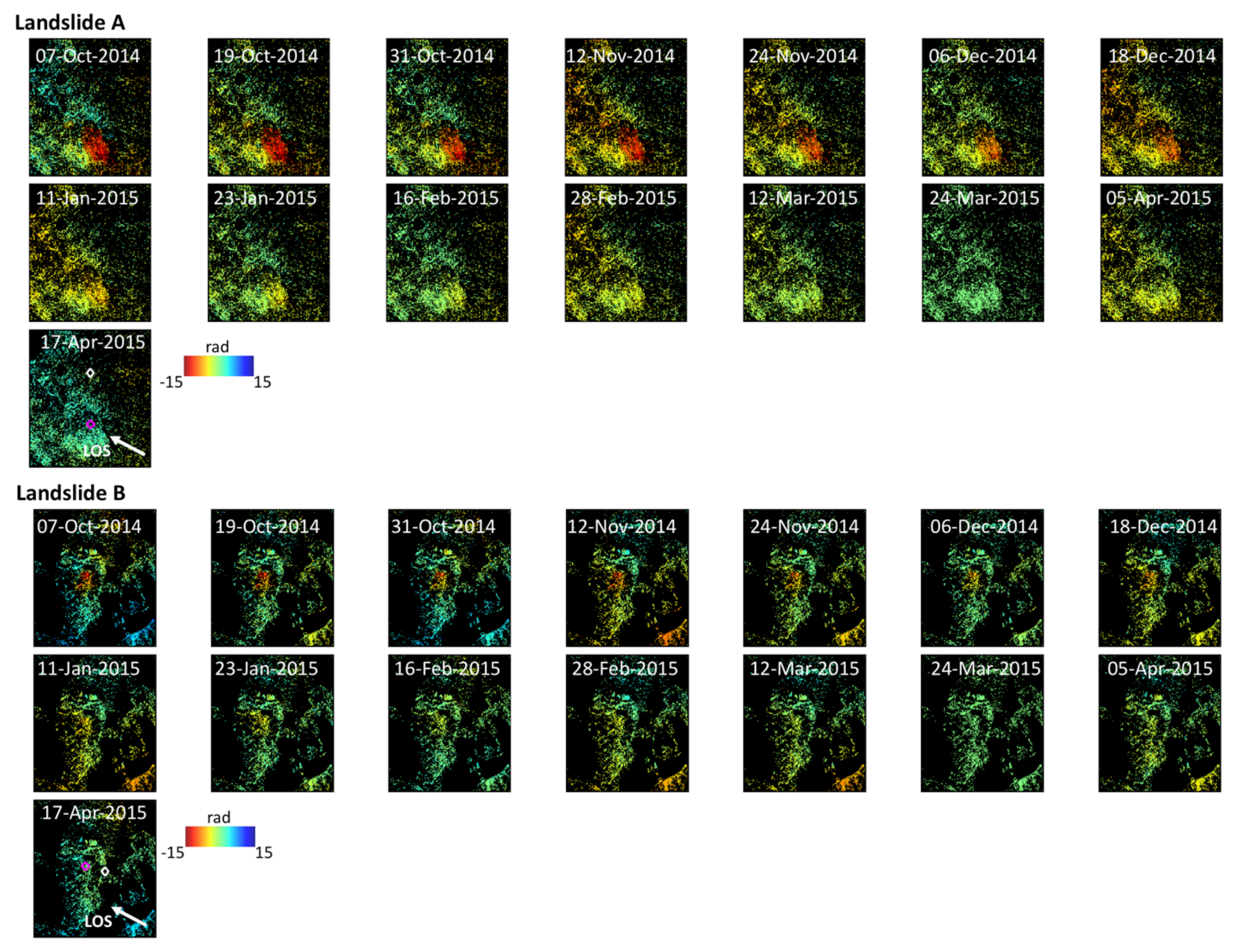


***Figure S6:*** *Line-of-sight displacement time-series for landslides A-F (located by the magenta marker) with respect to their stable reference point (white diamond) for the pre-Gorka period. Time-series shows cumulative displacement relative to 24 March 2015, where 6.28 radians corresponds to approximately 2.6 cm of displacement in the radar line-of-sight. Boxes are approximately 4 km by 4 km in size.*

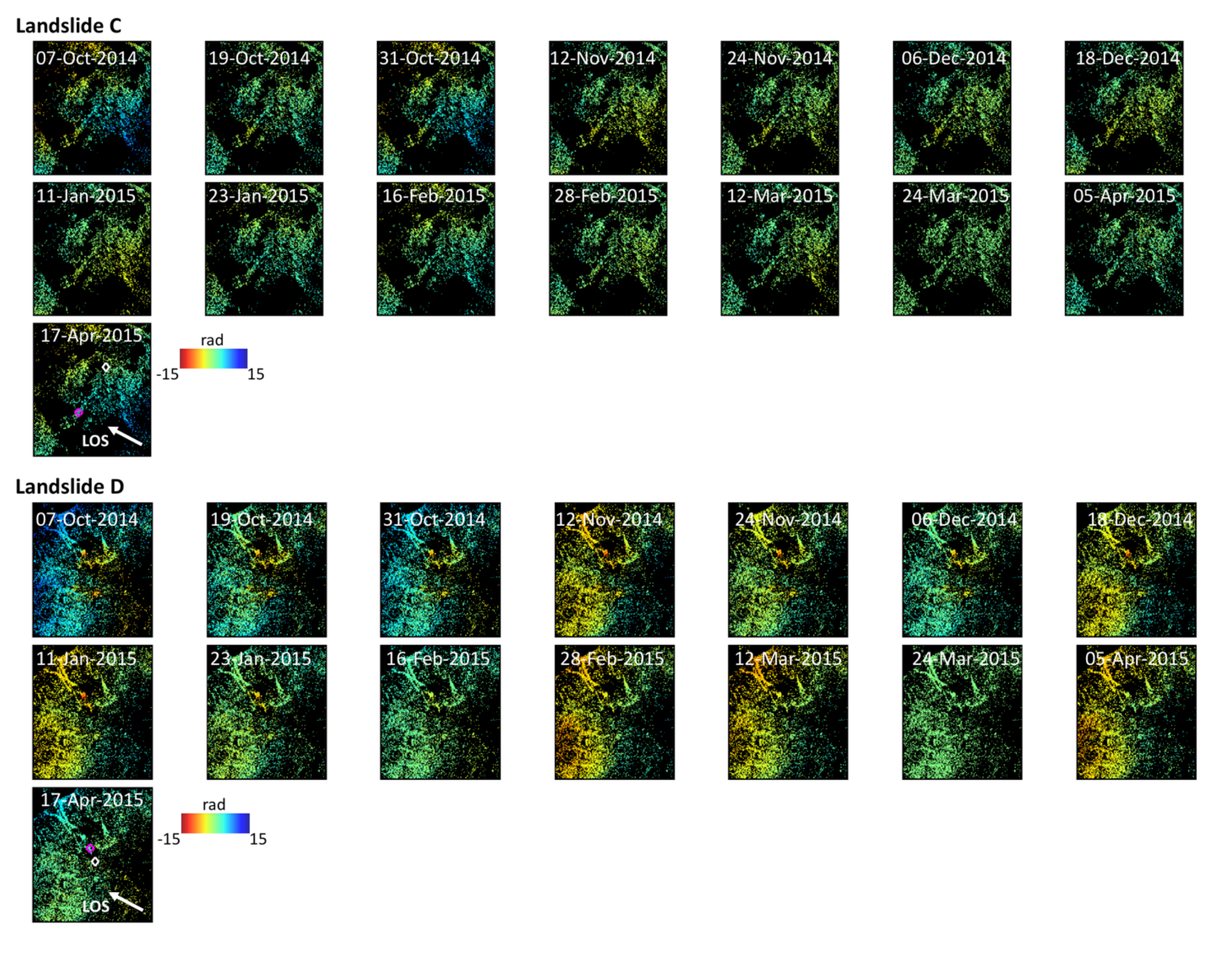


***Figure S6:*** *Cont.*

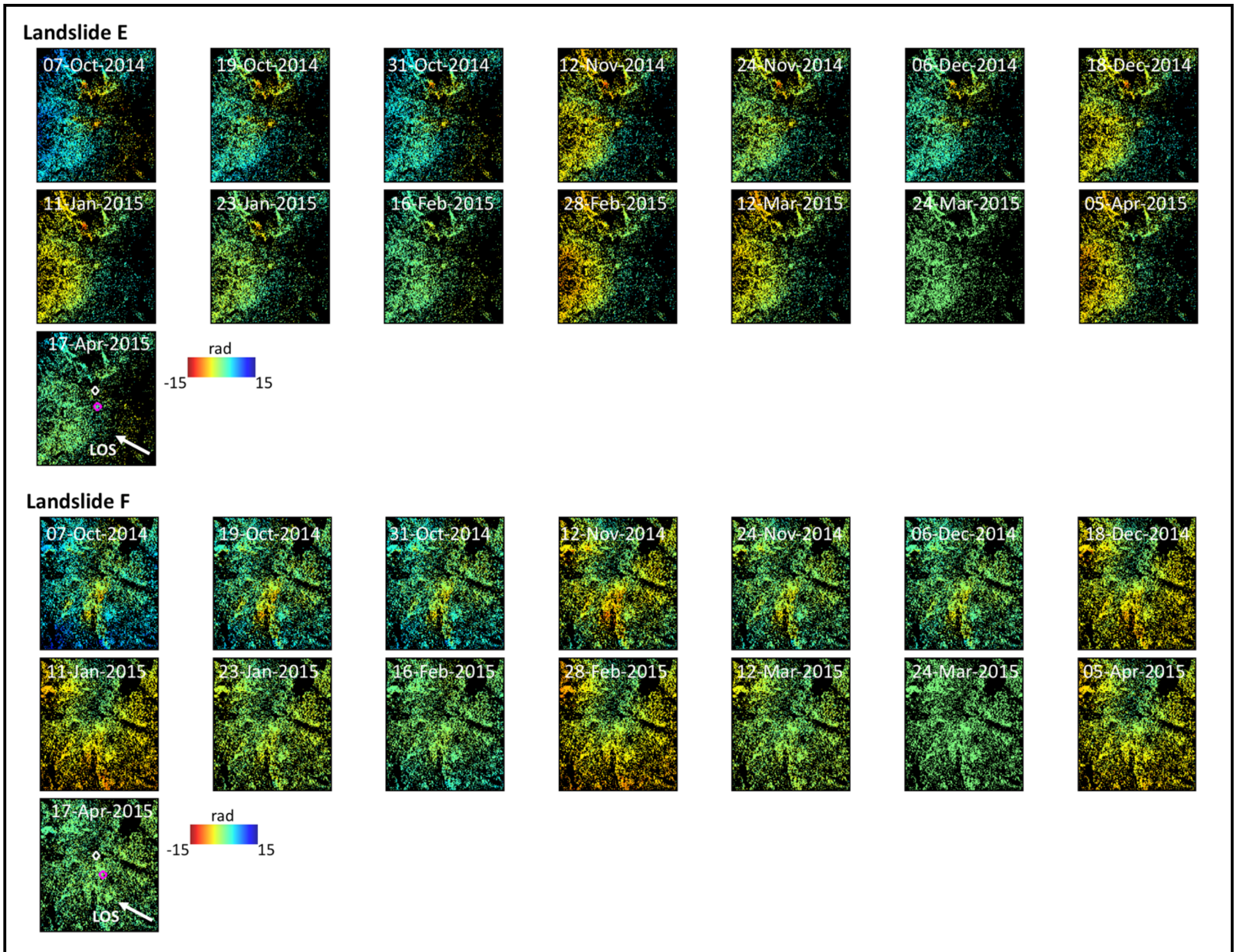


***Figure S6:*** *Cont.*

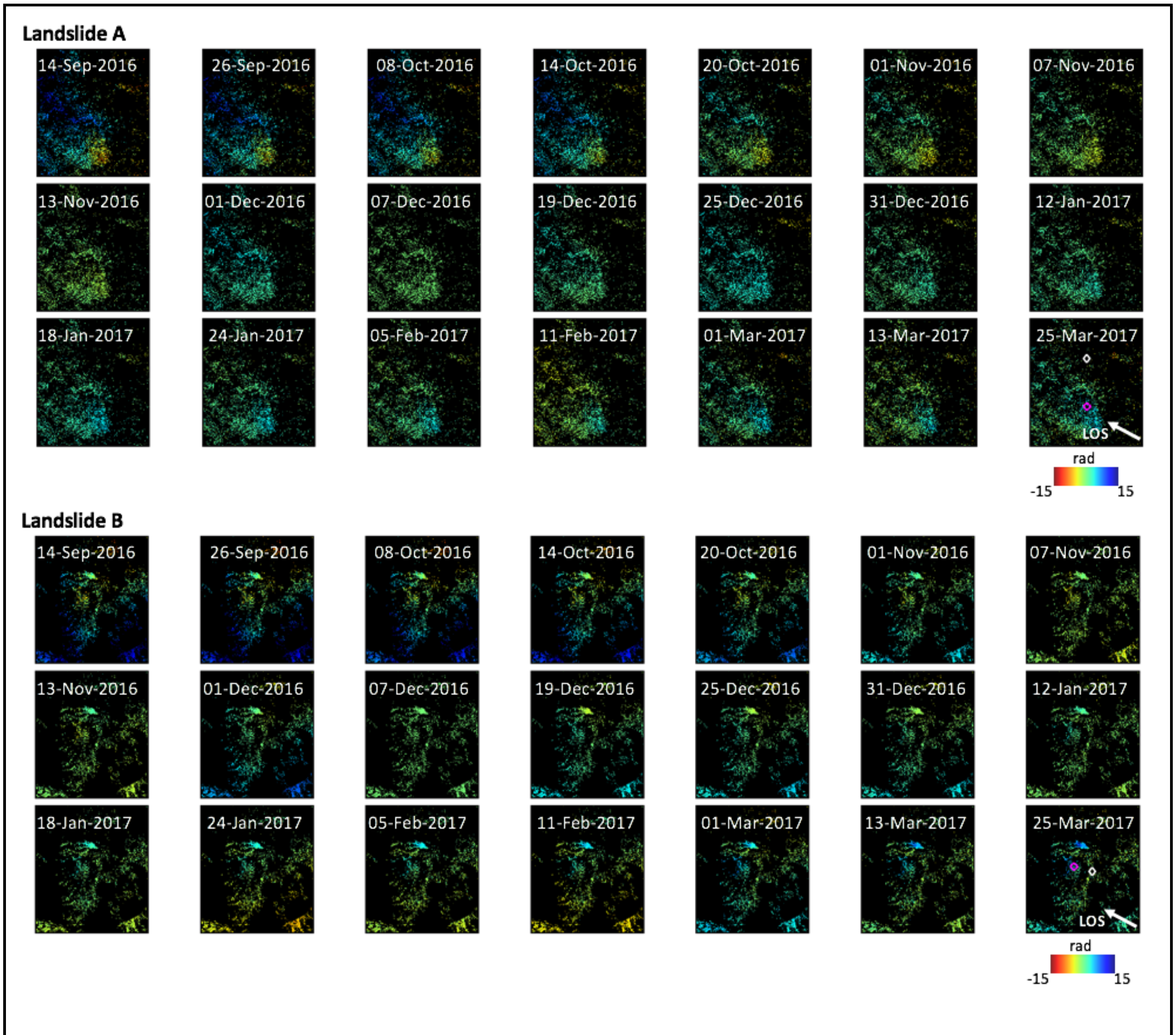


***Figure S7:*** *Line-of-sight displacement time-series for landslides A-F (located by the magenta marker) with respect to their stable reference point (white diamond) for the post-Gorka period. Time-series shows cumulative displacement relative to 7 December 2017, where 6.28 radians corresponds to approximately 2.6 cm of displacement in the radar line-of-sight. Boxes are approximately 4 km by 4 km in size.*

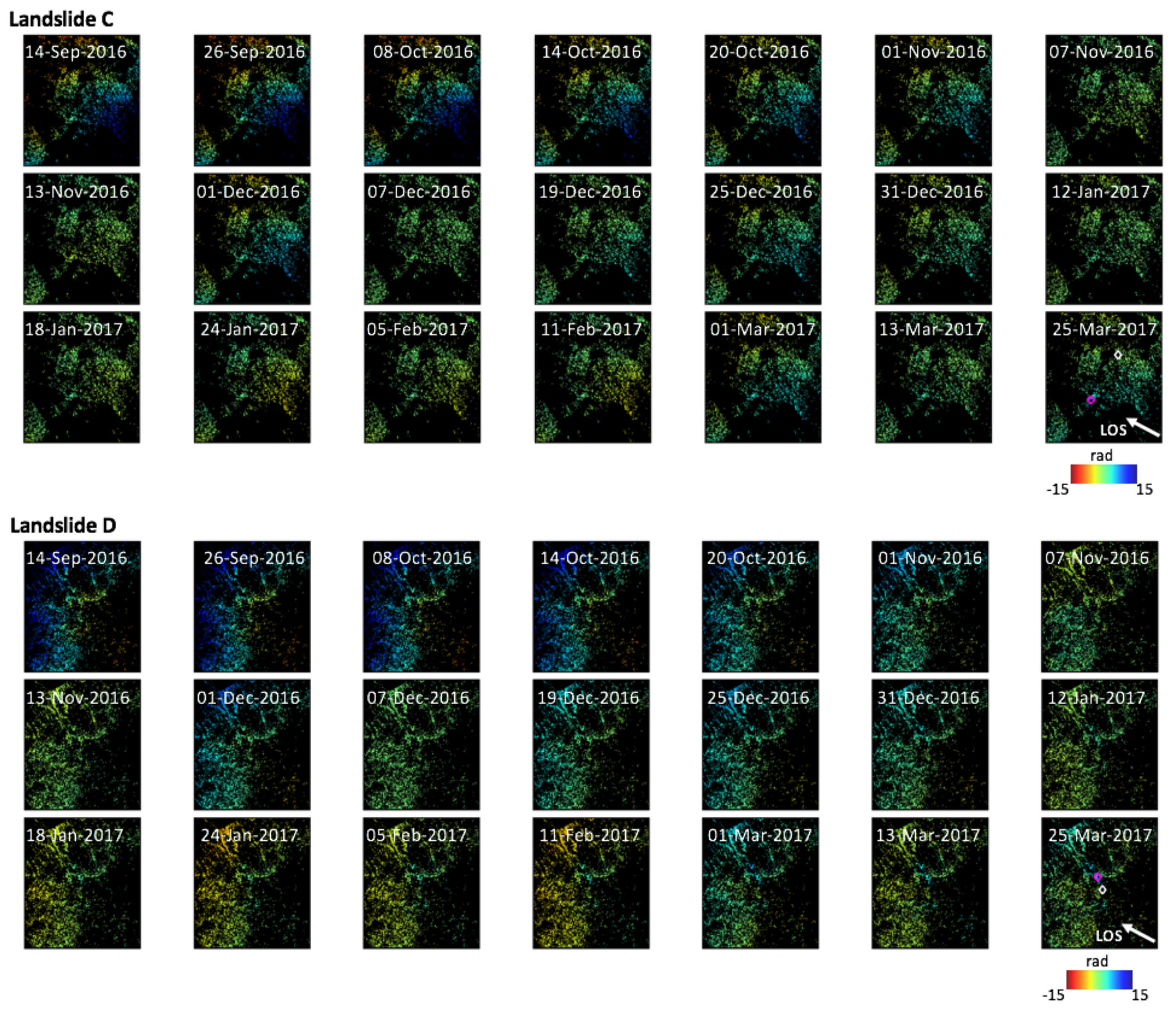


***Figure S7:*** *Cont.*

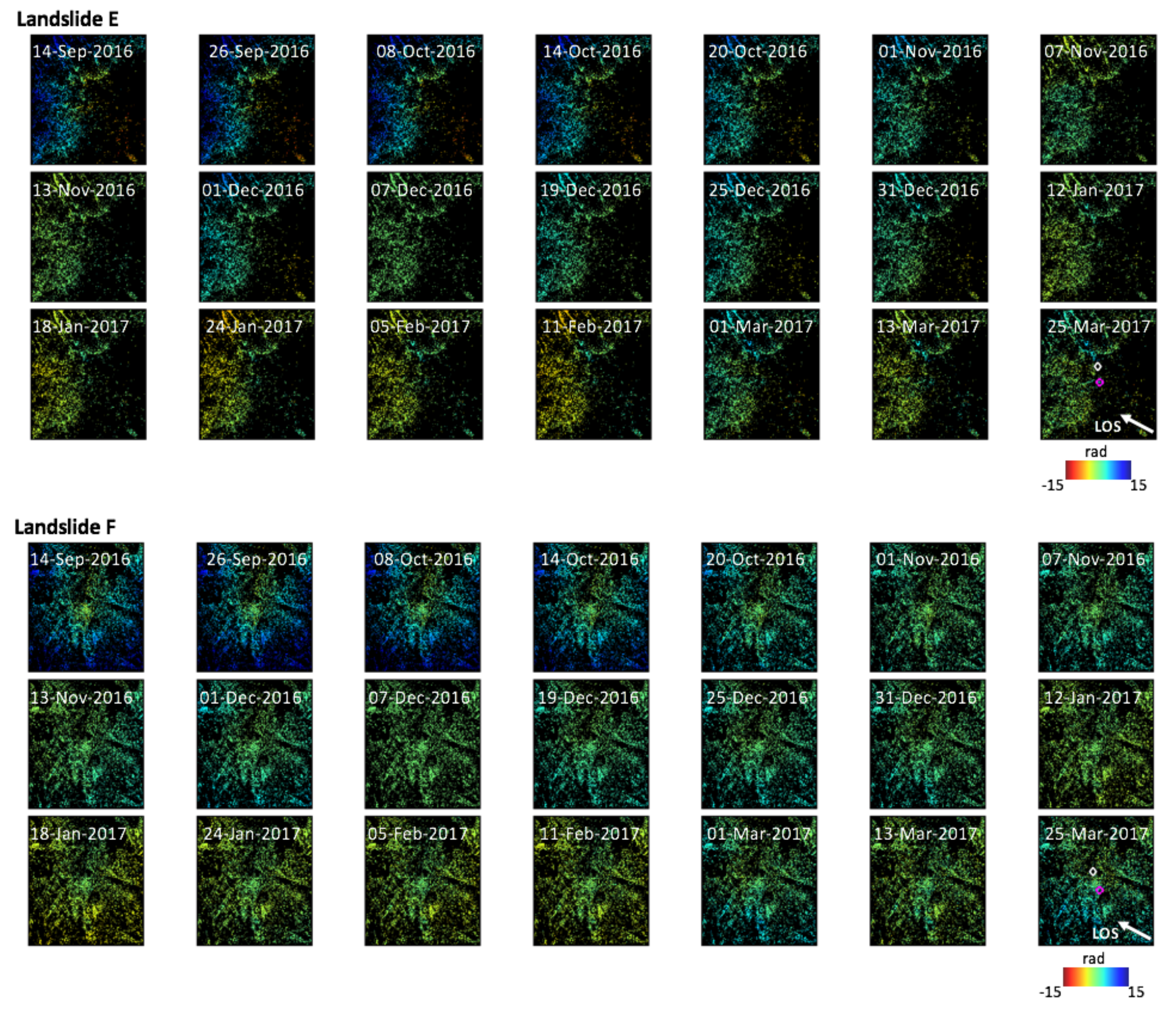


***Figure S7:*** *Cont.*

# Supplemental Tables

***Table S1***: *Landslide statistics. Planform area (km$^2$) is calculated as the area within the landslide polygon (**Figure 4**). Length (m) is calculated as the distance from the top to the bottom of the landslide along the longitudinal axis. Average width (m) is calculated as Area/Length.*

| Landslide name | Area (km$^2$) | Length (m) | Width (m) | Mean Elevation (km) | Mean Slope (deg) | Min Slope (deg) | Max Slope (deg) | 2014 Mean LOS Velocity (mm/yr) | 2016 Mean LOS Velocity (mm/yr) |
|---|---|---|---|---|---|---|---|---|---|
| A | 1.14 | 1552 | 736 | 2.31 | 16.6 | 10.5 | 29.1 | -88.5±7.9 | -66.6±7.0 |
| B | 0.5 | 728 | 695 | 2.01 | 24.6 | 16.2 | 33.4 | -56.2±4.5 | -47.6±3.7 |
| C | 1.37 | 2045 | 669 | 2.17 | 25.5 | 18.3 | 34.4 | -30.9±6.5 | -23.3±6.9 |
| D | 0.39 | 490 | 795 | 2.23 | 25.8 | 22 | 31 | -39.0±6.5 | -28.2±3.5 |
| E | 1.66 | 2748 | 605 | 1.75 | 27.5 | 18.1 | 50.1 | -36.9±2.1 | -36.2 ± 3.0 |
| F | 0.85 | 1296 | 652 | 2.05 | 23.2 | 13.8 | 29.2 | -26.8±6.0 | -21.1±4.0 |

***Table S2***: *Overview of interferometric pairs and their corresponding perpendicular baseline as used in our time-series InSAR analysis.*

| ID | Interferogram pair | Perp. Baseline | ID | Interferogram pair | Perp. Baseline |
|---|---|---|---|---|---|
| 1 | 20141007-20141019 | -36.42 | 75 | 20160306-20160610 | -67.69 |
| 2 | 20141007-20141031 | -113.68 | 76 | 20160330-20160517 | -5.87 |
| 3 | 20141019-20141031 | -77.26 | 77 | 20160330-20160610 | -7.98 |
| 4 | 20141019-20141112 | 2.3 | 78 | 20160330-20160728 | -89.39 |
| 5 | 20141019-20141124 | 125.98 | 79 | 20160517-20160610 | -2.11 |
| 6 | 20141019-20141206 | 84.84 | 80 | 20160517-20160728 | -83.52 |
| 7 | 20141019-20141218 | 50.53 | 81 | 20160517-20160821 | 69.59 |
| 8 | 20141031-20141112 | 79.56 | 82 | 20160610-20160728 | -81.41 |
| 9 | 20141031-20141124 | 203.24 | 83 | 20160610-20160821 | 71.7 |
| 10 | 20141031-20141206 | 162.1 | 84 | 20160610-20160914 | 25.58 |
| 11 | 20141112-20141124 | 123.68 | 85 | 20160728-20160821 | 153.11 |
| 12 | 20141112-20141206 | 82.54 | 86 | 20160728-20160914 | 106.99 |
| 13 | 20141112-20141218 | 48.23 | 87 | 20160728-20160926 | 156.52 |
| 14 | 20141112-20150111 | 66.6 | 88 | 20160821-20160914 | -46.12 |
| 15 | 20141124-20141206 | -41.14 | 89 | 20160821-20160926 | 3.41 |
| 16 | 20141124-20141218 | -75.45 | 90 | 20160821-20161008 | -18.71 |
| 17 | 20141124-20150111 | -57.08 | 91 | 20160914-20160926 | 49.53 |
| 18 | 20141124-20150123 | 1.01 | 92 | 20160914-20161008 | 27.41 |
| 19 | 20141206-20141218 | -34.31 | 93 | 20160914-20161014 | 27.83 |
| 20 | 20141206-20150111 | -15.94 | 94 | 20160926-20161008 | -22.12 |
| 21 | 20141206-20150123 | 42.15 | 95 | 20160926-20161014 | -21.7 |
| 22 | 20141206-20150216 | -60.4 | 96 | 20160926-20161020 | -88.4 |
| 23 | 20141218-20150111 | 18.37 | 97 | 20161008-20161014 | 0.42 |
| 24 | 20141218-20150123 | 76.46 | 98 | 20161008-20161020 | -66.28 |

| | | |
|---|---|---|
| 25 | 20141218-20150216 | -26.09 |
| 26 | 20150111-20150228 | -119.74 |
| 27 | 20150123-20150216 | -102.55 |
| 28 | 20150216-20150228 | -75.28 |
| 29 | 20150216-20150312 | -104.36 |
| 30 | 20150216-20150324 | -45.16 |
| 31 | 20150216-20150405 | 12.47 |
| 32 | 20150216-20150417 | -9.23 |
| 33 | 20150228-20150312 | -29.08 |
| 34 | 20150228-20150405 | 87.75 |
| 35 | 20150312-20150405 | 116.83 |
| 36 | 20150324-20150417 | 35.93 |
| 37 | 20150429-20150511 | -44.99 |
| 38 | 20150429-20150523 | -55.18 |
| 39 | 20150429-20150604 | 41.26 |
| 40 | 20150511-20150523 | -10.19 |
| 41 | 20150511-20150604 | 86.25 |
| 42 | 20150511-20150628 | 124.26 |
| 43 | 20150523-20150604 | 96.44 |
| 44 | 20150523-20150628 | 134.45 |
| 45 | 20150523-20150710 | -118.77 |
| 46 | 20150604-20150628 | 38.01 |
| 47 | 20150604-20150710 | -215.21 |
| 48 | 20150604-20150722 | -64.54 |
| 49 | 20150628-20150710 | -253.22 |
| 50 | 20150628-20150722 | -102.55 |
| 51 | 20150628-20150815 | -99.34 |
| 52 | 20150710-20150722 | 150.67 |
| 99 | 20161008-20161101 | 42.01 |
| 100 | 20161014-20161020 | -66.7 |
| 101 | 20161014-20161101 | 41.59 |
| 102 | 20161014-20161107 | 23.51 |
| 103 | 20161020-20161101 | 108.29 |
| 104 | 20161020-20161107 | 90.21 |
| 105 | 20161020-20161113 | 63.03 |
| 106 | 20161101-20161107 | -18.08 |
| 107 | 20161101-20161113 | -45.26 |
| 108 | 20161101-20161201 | -0.8 |
| 109 | 20161107-20161113 | -27.18 |
| 110 | 20161107-20161201 | 17.28 |
| 111 | 20161107-20161207 | -17.93 |
| 112 | 20161113-20161201 | 44.46 |
| 113 | 20161113-20161207 | 9.25 |
| 114 | 20161113-20161219 | 26.59 |
| 115 | 20161201-20161207 | -35.21 |
| 116 | 20161201-20161219 | -17.87 |
| 117 | 20161201-20161225 | -17.74 |
| 118 | 20161207-20161219 | 17.34 |
| 119 | 20161207-20161225 | 17.47 |
| 120 | 20161207-20161231 | 91.77 |
| 121 | 20161219-20161225 | 0.13 |
| 122 | 20161219-20161231 | 74.43 |
| 123 | 20161219-20170112 | 26.13 |
| 124 | 20161225-20161231 | 74.3 |
| 125 | 20161225-20170112 | 26 |
| 126 | 20161225-20170118 | -64.31 |

| | | |
|---|---|---|
| 53 | 20150710-20150815 | 153.88 |
| 54 | 20150710-20150827 | 181.34 |
| 55 | 20150722-20150815 | 3.21 |
| 56 | 20150722-20150827 | 30.67 |
| 57 | 20150722-20150908 | -13.16 |
| 58 | 20150815-20150827 | 27.46 |
| 59 | 20150815-20150908 | -16.37 |
| 60 | 20150815-20151107 | -61.98 |
| 61 | 20150827-20150908 | -43.83 |
| 62 | 20150827-20151107 | -89.44 |
| 63 | 20150827-20160211 | -78.77 |
| 64 | 20150908-20151107 | -45.61 |
| 65 | 20150908-20160211 | -34.94 |
| 66 | 20150908-20160306 | 38.59 |
| 67 | 20151107-20160211 | 10.67 |
| 68 | 20151107-20160306 | 84.2 |
| 69 | 20151107-20160330 | 24.49 |
| 70 | 20160211-20160306 | 73.53 |
| 71 | 20160211-20160330 | 13.82 |
| 72 | 20160211-20160517 | 7.95 |
| 73 | 20160306-20160330 | -59.71 |
| 74 | 20160306-20160517 | -65.58 |

| | | |
|---|---|---|
| 127 | 20161231-20170112 | -48.3 |
| 128 | 20161231-20170118 | -138.61 |
| 129 | 20161231-20170124 | -125.61 |
| 130 | 20170112-20170118 | -90.31 |
| 131 | 20170112-20170124 | -77.31 |
| 132 | 20170112-20170205 | -85.76 |
| 133 | 20170118-20170124 | 13 |
| 134 | 20170118-20170205 | 4.55 |
| 135 | 20170118-20170211 | 104.88 |
| 136 | 20170124-20170205 | -8.45 |
| 137 | 20170124-20170211 | 91.88 |
| 138 | 20170124-20170301 | -36.44 |
| 139 | 20170205-20170211 | 100.33 |
| 140 | 20170205-20170301 | -27.99 |
| 141 | 20170205-20170313 | 70.78 |
| 142 | 20170211-20170301 | -128.32 |
| 143 | 20170211-20170313 | -29.55 |
| 144 | 20170211-20170325 | -96.59 |
| 145 | 20170301-20170313 | 98.77 |
| 146 | 20170301-20170325 | 31.73 |
| 147 | 20170313-20170325 | -67.04 |

Table S3: Processing workflow. Star indicates processing steps that are carried out for the pre- and post Gorkha earthquake periods separately.

| Step | Processing Description | Data Output |
|---|---|---|
| 1 | ISCE TOPS Stack processor | Coregistered SLC stack |
| 2* | ISCE2StaMPS | Unwrapped Small Baseline Interferograms |
| 3* | StaMPS Small Baseline method up to unwrapping stage | |
| 4* | Mask out pixels over flat terrain (slope < 5 degrees) and those that are in shadow or lay-over | |
| 5* | Local and regional filtering of SB interferograms | Double differenced unwrapped Small Baseline Interferograms |
| 6* | StaMPS time-series analysis | Double Difference “rate”($\Delta V_{LOS}$) and “rate uncertainty” ($\sigma_{\Delta V_{LOS}}$) |
| 7* | Thresholding to only show significant local processes $\lvert\Delta V_{LOS}\rvert - 2\sigma_{\Delta V_{LOS}} > 0$ | Cluster map of significant local processes |
| 8* | Clustering requiring minimum of 3 pixels per cluster | |

# References


Ader, T., Avouac, J.-P., Liu-Zeng, J., Lyon-Caen, H., Bollinger, L., Galetzka, J., Genrich, J., Thomas, M., Chanard, K., Sapkota, S.N., Rajaure, S., Shrestha, P., Ding, L. & Flouzat, M., 2012. Convergence rate across the Nepal Himalaya and interseismic coupling on the Main Himalayan Thrust: Implications for seismic hazard, Journal of Geophysical Research: Solid Earth, 117, B04403.

Agliardi, F., Scuderi, M. M., Fusi, N., & Collettini, C. (2020). Slow-to-fast transition of giant creeping rockslides modulated by undrained loading in basal shear zones. Nature communications, 11(1), 1-11.

Amelung, F., S. Jonsson, H. Zebker, and P. Segall (2000), Widespread uplift and /`trapdoor/’ faulting on Galapagos volcanoes observed with radar interferometry, Nature, 407(6807), 993–996.

Ansari, H., De Zan, F. and Bamler, R., 2017. Sequential estimator: Toward efficient InSAR time series analysis. IEEE Transactions on Geoscience and Remote Sensing, 55(10), pp.5637-5652.

Bekaert, D. P., Jones, C. E., An, K., & Huang, M. H. (2019). Exploiting UAVSAR for a comprehensive analysis of subsidence in the Sacramento Delta. *Remote sensing of environment*, *220*, 124-134.

Bekaert, D.P.S., B. D. Hamlington, B. Buzzanga, and C. E. Jones (2017), Spaceborne Synthetic Aperture Radar Survey of Subsidence in Hampton Roads, Virginia (USA), Scientific Reports, doi:10.1038/s41598-017-15309-5.

Bekaert, D.P.S., Hooper, A. and Wright, T.J., (2015c). Reassessing the 2006 Guerrero slow-slip event, Mexico: Implications for large earthquakes in the Guerrero Gap. Journal of Geophysical Research: Solid Earth, 120(2), pp.1357-1375.

Bekaert, D.P.S., R.J. Walters, T.J. Wright, A.J. Hooper, and D.J. Parker (2015b) Statistical comparison of InSAR tropospheric correction techniques, Remote Sensing of Environment, doi:10.1016/j.rse.2015.08.035.

Bekaert D.P.S., A. Hooper, and T.J. Wright (2015a), A spatially-variable power-law tropospheric correction technique for InSAR data, JGR, doi:10.1029/2014JB011558

Bilham, R., 2004. Earthquakes in India and the Himalaya: tectonics, geodesy and history. Annals of GEOPHYSICS.

Bontemps, N., Lacroix, P., Larose, E., Jara, J., & Taipe, E. (2020). Rain and small earthquakes maintain a slow-moving landslide in a persistent critical state. Nature Communications, 11(1), 1-10.

Booth, A. M., McCarley, J., Hinkle, J., Shaw, S., Ampuero, J. P., & Lamb, M. P. (2018). Transient Reactivation of a Deep-Seated Landslide by Undrained Loading Captured With Repeat Airborne and Terrestrial Lidar. *Geophysical Research Letters*, *45*(10), 4841-4850.

Buzzanga, B. A., Bekaert, D. P. S., Hamlington, B. D., and Sanga, S. (in review). Towards Sustained Monitoring of Subsidence at the Coast using InSAR and GNSS: An Application in Hampton Roads, Virginia. Geophysical Research Letters.

Caine, N., & Mool, P. K. (1982). Landslides in the Kolpu Khola drainage, middle mountains, Nepal. *Mountain Research and Development*, 157-173.

Carrière, S. R., Jongmans, D., Chambon, G., Bièvre, G., Lanson, B., Bertello, L., Berti, M., Jaboyedoff, M., Malet, J-P., and Chambers, J. E. (2018). Rheological properties of clayey soils originating from flow-like landslides. Landslides, 15(8), 1615-1630.

Casey, K. A., A. Kääb, and D. I. Benn (2012), Geochemical characterization of supraglacial debris via in situ and optical remote sensing methods: a case study in Khumbu Himalaya, Nepal, Cryosph., 6(1), 85–100, doi:10.5194/tc-6-85-2012.

Colesanti, C., A. Ferretti, C. Prati, and F. Rocca (2003), Monitoring landslides and tectonic motions with the Permanent Scatterers Technique, Eng. Geol., 68(1–2), 3–14, doi:http://dx.doi.org/10.1016/S0013-7952(02)00195-3.

Collins, B.D. and Jibson, R.W., 2015. Assessment of existing and potential landslide hazards resulting from the April 25, 2015 Gorkha, Nepal earthquake sequence (No. 2015-1142). US Geological Survey.

Coe, J. A., McKenna, J. P., Godt, J. W., & Baum, R. L. (2009). Basal-topographic control of stationary ponds on a continuously moving landslide. *Earth Surface Processes and Landforms*, *34*(2), 264-279.

Liang, C., Liu, Z., Fielding, E. J., & Bürgmann, R. (2018). InSAR time series analysis of L-Band wide-swath SAR data acquired by ALOS-2. *IEEE Transactions on Geoscience and Remote Sensing*, *56*(8), 4492-4506.

Dahal, R. K., & Hasegawa, S. (2008). Representative rainfall thresholds for landslides in the Nepal Himalaya. Geomorphology, 100(3-4), 429-443.

Dai, K., Xu, Q., Li, Z., Tomás, R., Fan, X., Dong, X., Li, W., Zhou, Z., Gou, J. and Ran, P., 2019. Post-disaster assessment of 2017 catastrophic Xinmo landslide (China) by spaceborne SAR interferometry. Landslides, pp.1-11.

Dehls, J.F., Larsen, Y., Marinkovic, P. and Moldestad, D.A., 2017, April. InSAR. no: First results from the Norwegian national deformation mapping service. In EGU General Assembly Conference Abstracts (Vol. 19, p. 3650).

Delbridge, B. G., Bürgmann, R., Fielding, E., Hensley, S., & Schulz, W. H. (2016). Three-dimensional surface deformation derived from airborne interferometric UAVSAR: Application to the Slumgullion Landslide. *Journal of geophysical research: solid earth*, *121*(5), 3951-3977.

Dhital, M.R., 2015. Geology of the Nepal Himalaya: regional perspective of the classic collided orogen. Springer.

Dille, A., Kervyn, F., Bibentyo, T. M., Delvaux, D., Ganza, G. B., Mawe, G. I., Buzera, G.K., Nakito, E.S., Moeyersons, J., Monsieurs, E. , Nzolang, C., Smets, B., Kervyn, M., and Dewitte, O. (2019). Causes and triggers of deep-seated hillslope instability in the tropics– Insights from a 60-year record of Ikoma landslide (DR Congo). Geomorphology, 345, 106835.

Elliott, J. R., Jolivet, R., González, P. J., Avouac, J.-P., Hollingsworth, J., Searle, M. P., Stevens, V. L., (2016), Himalayan megathrust geometry and relation to topography revealed by the Gorkha earthquake, Nature Geoscience, volume 9, pages 174–180 , doi:10.1038/ngeo2623

Farr, T.G., Rosen, P.A., Caro, E., Crippen, R., Duren, R., Hensley, S., Kobrick, M., Paller, M., Rodriguez, E., Roth, L., Seal, D., Shaffer, S., Shimada, J., Umland, J., Werner, M., Oskin, M., Burbank, D., Alsdorf, D., 2007. The Shuttle Radar Topography Mission. Rev. Geophys. 45. https://doi.org/10.1029/2005RG000183

Fattahi, H., P. Agram, and M. Simons (2017), A Network-Based Enhanced Spectral Diversity Approach for TOPS Time-Series Analysis, IEEE Transactions on Geoscience and Remote Sensing, Vol 55.

Ferretti, A., Fumagalli, A., Novali, F., Prati, C., Rocca, F., Rucci, A., 2011. A New Algorithm for Processing Interferometric Data-Stacks: SqueeSAR. IEEE Trans. Geosci. Remote Sens. 49, 3460–3470. https://doi.org/10.1109/TGRS.2011.2124465.

Ferretti, A., Prati, C., Rocca, F., 2001. Permanent scatterers in SAR interferometry. IEEE Trans. Geosci. Remote Sens. 39, 8–20. https://doi.org/10.1109/36.898661.Fielding, E.J., Sangha, S.S., Bekaert, D.P., Samsonov, S.V. and Chang, J.C., 2017. Surface deformation of north-central Oklahoma related to the 2016 M w 5.8 Pawnee earthquake from SAR interferometry time series. Seismological Research Letters, 88(4), pp.971-982.

Froude, M. J., & Petley, D. (2018). Global fatal landslide occurrence from 2004 to 2016. *Natural Hazards and Earth System Sciences*, *18*, 2161-2181.

Gariano, S. L., & Guzzetti, F. (2016). Landslides in a changing climate. Earth-Science Reviews, 162, 227-252.

Geertsema, M., Schwab, J. W., Blais-Stevens, A., & Sakals, M. E. (2009). Landslides impacting linear infrastructure in west central British Columbia. *Natural Hazards*, *48*(1), 59-72.

Guerriero, L., Bertello, L., Cardozo, N., Berti, M., Grelle, G., & Revellino, P. (2017). Unsteady sediment discharge in earth flows: A case study from the Mount Pizzuto earth flow, southern Italy. Geomorphology, 295, 260-284.

Handwerger, A.L., Huang, M-H., Fielding, E.J., Booth, A.M., Bürgmann, R. (2019a), A shift from drought to extreme rainfall drives a stable landslide to catastrophic failure, Scientific Reports, 9, doi:10.1038/s41598-018-38300-0

Handwerger, A. L., Rempel, A. W., Skarbek, R. M., Roering, J. J., & Hilley, G. E. (2016). Rate-weakening friction characterizes both slow sliding and catastrophic failure of landslides. *Proceedings of the National Academy of Sciences*, *113*(37), 10281-10286.

Handwerger, A.L., Roering, J.J. and Schmidt, D.A., 2013. Controls on the seasonal deformation of slow-moving landslides. Earth and Planetary Science Letters, 377, pp.239-247.

Handwerger, A. L., Roering, J. J., Schmidt, D. A., & Rempel, A. W. (2015). Kinematics of earthflows in the Northern California Coast Ranges using satellite interferometry. *Geomorphology*, *246*, 321-333.

Handwerger, A. L., Fielding, E. J., Huang, M. H., Bennett, G. L., Liang, C., & Schulz, W. H. (2019b). Widespread initiation, reactivation, and acceleration of landslides in the northern California Coast Ranges due to extreme rainfall. *Journal of Geophysical Research: Earth Surface*.

Herrera, G., Gutiérrez, F., García-Davalillo, J. C., Guerrero, J., Notti, D., Galve, J. P., ... & Cooksley, G. (2013). Multi-sensor advanced DInSAR monitoring of very slow landslides: The Tena Valley case study (Central Spanish Pyrenees). *Remote Sensing of Environment*, *128*, 31-43

Hilley, G. E., Bürgmann, R., Ferretti, A., Novali, F., & Rocca, F. (2004). Dynamics of slow-moving landslides from permanent scatterer analysis. Science, 304(5679), 1952-1955.

Hooper, A., D. Bekaert, K. Spaans and M. Arikan (2012), Recent advances in SAR interferometry time series analysis for measuring crustal deformation, Tectonophysics, 514-517, 1-13, doi:10.1016/j.tecto.2011.10.013.

Hooper, A., Zebker, H., Segall, P., Kampes, B., (2004). A new method for measuring deformation on volcanoes and other natural terrains using InSAR persistent scatterers. Geophys. Res. Lett. 31, L23611. https://doi.org/10.1029/2004GL021737

Huang, M.-H., R. Bürgmann, and J.-C., Hu (2016). Fifteen years of surface deformation in southwestern Taiwan: Insight from SAR interferometry, Tectonophysics, http://dx.doi.org/10.1016/j.tecto.2016.02.021.

Huang, M.H., Fielding, E.J., Liang, C., Milillo, P., Bekaert, D., Dreger, D. and Salzer, J., 2017. Coseismic deformation and triggered landslides of the 2016 Mw 6.2 Amatrice earthquake in Italy. Geophysical Research Letters, 44(3), pp.1266-1274.

Huffman, G. (2017), GPM IMERG Final Precipitation L3 1 day 0.1 degree x 0.1 degree V05, Edited by Andrey Savtchenko, Greenbelt, MD, Goddard Earth Sciences Data and Information Services Center (GES DISC), Accessed: 18 February 2019, doi:10.5067/GPM/IMERGDF/DAY/05

Hungr, O., Leroueil, S., & Picarelli, L. (2014). The Varnes classification of landslide types, an update. *Landslides*, *11*(2), 167-194.

Hussain, E., Hooper, A., Wright, T. J., Walters, R. J., & Bekaert, D. P. (2016). Interseismic strain accumulation across the central North Anatolian Fault from iteratively unwrapped InSAR measurements. Journal of Geophysical Research: Solid Earth, 121(12), 9000-9019.

Intrieri, E. et al. The maoxian landslide as seen from space: detecting precursors of failure with sentinel-1 data. Landslides 15, 123–133 (2018)

Jolivet, R., Grandin, R., Lasserre, C., Doin, M. P., & Peltzer, G. (2011). Systematic InSAR tropospheric phase delay corrections from global meteorological reanalysis data. Geophysical Research Letters, 38(17).

Jones, C.E., An, K., Blom, R.G., Kent, J.D., Ivins, E.R. and Bekaert, D., 2016. Anthropogenic and geologic influences on subsidence in the vicinity of New Orleans, Louisiana. Journal of Geophysical Research: Solid Earth, 121(5), pp.3867-3887.

Kargel, J.S., Leonard, G.J., Shugar, D.H., Haritashya, U.K., Bevington, A., Fielding, E.J., Fujita, K., Geertsema, M., Miles, E.S., Steiner, J. and Anderson, E., 2016. Geomorphic and geologic controls of geohazards induced by Nepal's 2015 Gorkha earthquake. Science, 351(6269), p.aac8353.

Kelsey, H. M. (1980). A sediment budget and an analysis of geomorphic process in the Van Duzen River basin, north coastal California, 1941–1975. Geological Society of America Bulletin, 91(4_Part_II), 1119-1216.Kilburn, C. R., & Petley, D. N. (2003). Forecasting giant, catastrophic slope collapse: lessons from Vajont, Northern Italy. Geomorphology, 54(1-2), 21-32.

Kirschbaum, D., & Stanley, T. ( 2018). Satellite-Based Assessment of Rainfall-Triggered Landslide Hazard for Situational Awareness. *Earth's Future*, 6, 505– 523. https://doi.org/10.1002/2017EF000715

Kirschbaum, D. B., T. Stanley, and Y. Zhou (2015), Spatial and Temporal Analysis of a Global Landslide Catalog, Geomorphology, doi:10.1016/j.geomorph.2015.03.016.

Kirschbaum, D. B., R. Adler, Y. Hong, S. Hill, and A. Lerner-Lam (2010), A global landslide catalog for hazard applications: method, results, and limitations, Nat. Hazards, 52(3), 561–575, doi:10.1007/s11069-009-9401-4.

Korup, O., Densmore, A. L., & Schlunegger, F. (2010). The role of landslides in mountain range evolution. Geomorphology, 120(1-2), 77-90.

Lacroix, P. (2016). Landslides triggered by the Gorkha earthquake in the Langtang valley, volumes and initiation processes. Earth, Planets Sp. 68, 46. doi:10.1186/s40623-016-0423-3.

Lacroix, P., Berthier, E. and Maquerhua, E.T., 2015. Earthquake-driven acceleration of slow-moving landslides in the Colca valley, Peru, detected from Pléiades images. *Remote Sensing of Environment*, *165*, pp.148-158.

Lacroix, P., Perfettini, H., Taipe, E., & Guillier, B. (2014). Coseismic and postseismic motion of a landslide: Observations, modeling, and analogy with tectonic faults. Geophysical Research Letters, 41(19), 6676-6680.

Larsen, I. J., Montgomery, D. R., & Korup, O. (2010). Landslide erosion controlled by hillslope material. Nature Geoscience, 3(4), 247.

Lavé, J. and Avouac, J.P., 2000. Active folding of fluvial terraces across the Siwaliks Hills, Himalayas of central Nepal. Journal of Geophysical Research: Solid Earth, 105(B3), pp.5735-5770.

Liang, C., P. Agram, M. Simons, and E. J. Fielding (2019), Ionospheric Correction of Insar Time Series Analysis of C-band Sentinel-1 TOPS Data, EarthArXiv, doi:10.31223/osf.io/atxr7.

Liao, H., Meyer, F.J., Scheuchl, B., Mouginot, J., Joughin, I. and Rignot, E., 2018. Ionospheric correction of InSAR data for accurate ice velocity measurement at polar regions. Remote sensing of environment, 209, pp.166-180.

Mansour, M. F., Morgenstern, N. R., & Martin, C. D. (2011). Expected damage from displacement of slow-moving slides. *Landslides*, *8*(1), 117-131.

Martha, T.R., Roy, P., Mazumdar, R., Govindharaj, K.B. and Kumar, K.V., 2017. Spatial characteristics of landslides triggered by the 2015 M w 7.8 (Gorkha) and M w 7.3 (Dolakha) earthquakes in Nepal. Landslides, 14(2), pp.697-704.

May, C., Roering, J., Eaton, L. S., & Burnett, K. M. (2013). Controls on valley width in mountainous landscapes: The role of landsliding and implications for salmonid habitat. Geology, 41(4), 503-506.

Merriam, R. Portuguese bend landslide, palos verdes hills, california. The Journal of Geology 68, 140–153 (1960).

Murray, K.D., D.P.S. Bekaert, R. B. Lohman (2019),Tropospheric corrections for InSAR: Statistical assessments and applications to the Central United States and Mexico, Remote Sensing of Environment, https://doi.org/10.1016/j.rse.2019.111326.

Nereson, A. L., & Finnegan, N. J. (2018). Drivers of earthflow motion revealed by an 80 yr record of displacement from Oak Ridge earthflow, Diablo Range, California, USA. *Bulletin*, *131*(3-4), 389-402.

Nichol, J., and M. S. Wong (2005), Satellite remote sensing for detailed landslide inventories using change detection and image fusion, Int. J. Remote Sens., 26(9), 1913–1926, doi:10.1080/01431160512331314047.

Oven, K. J. (2009), Landscape, Livelihoods and Risk: Community Vulnerability to Landslides in Nepal, Durham University.

Petley, D. N., G. J. Hearn, A. Hart, N. J. Rosser, S. A. Dunning, K. Oven, and W. A. Mitchell (2007), Trends in landslide occurrence in Nepal, Nat. Hazards, 43, 23–44, doi:10.1007/s11069-006-9100-3.

Scheingross, J. S., Minchew, B. M., Mackey, B. H., Simons, M., Lamb, M. P., & Hensley, S. (2013). Fault-zone controls on the spatial distribution of slow-moving landslides. *Bulletin*, *125*(3-4), 473-489.

Schulz, W. H., and Wang, G. (2014). Residual shear strength variability as a primary control on movement of landslides reactivated by earthquake-induced ground motion: Implications for coastal Oregon, US. Journal of Geophysical Research: Earth Surface, 119(7), 1617-1635.

Sella, G.F., Dixon, T.H. and Mao, A., 2002. REVEL: A model for recent plate velocities from space geodesy. Journal of Geophysical Research: Solid Earth, 107(B4), pp.ETG-11.

Shean, D. 2017. High Mountain Asia 8-meter DEM Mosaics Derived from Optical Imagery, Version 1. Boulder, Colorado USA. NASA National Snow and Ice Data Center Distributed Active Archive Center. doi: https://doi.org/10.5067/KXOVQ9L172S2

Shean, D. E., O. Alexandrov, Z. Moratto, B. E. Smith, I. R. Joughin, C. C. Porter, Morin, P. J. (2016), An automated, open-source pipeline for mass production of digital elevation models (DEMs) from very high-resolution commercial stereo satellite imagery, ISPRS J. Photogramm. Remote Sens, 116, 101–117, doi:10.1016/j.isprsjprs.2016.03.012.

Simoni, A., Ponza, A., Picotti, V., Berti, M., & Dinelli, E. (2013). Earthflow sediment production and Holocene sediment record in a large Apennine catchment. *Geomorphology*, *188*, 42-53.

Song, X.-P., J. O. Sexton, C. Huang, S. Channan, and J. R. Townshend (2016), Characterizing the magnitude, timing and duration of urban growth from time series of Landsat-based estimates of impervious cover, Remote Sens. Environ., 175, 1–13, doi:http://dx.doi.org/10.1016/j.rse.2015.12.027.

Strozzi, T., Klimeš, J., Frey, H., Caduff, R., Huggel, C., Wegmüller, U., & Rapre, A. C. (2018). Satellite SAR interferometry for the improved assessment of the state of activity of landslides: A case study from the Cordilleras of Peru. Remote sensing of environment, 217, 111-125.

Tantianuparp, P., X. Shi, L. Zhang, T. Balz, and M. Liao (2013), Characterization of Landslide Deformations in Three Gorges Area Using Multiple InSAR Data Stacks, Remote Sens. , 5(6), doi:10.3390/rs5062704.

Tsou, C.Y., Chigira, M., Higaki, D., Sato, G., Yagi, H., Sato, H.P., Wakai, A., Dangol, V., Amatya, S.C. and Yatagai, A., 2018. Topographic and geologic controls on landslides induced by the 2015 Gorkha earthquake and its aftershocks: an example from the Trishuli Valley, central Nepal. Landslides, pp.1-13.

Roback, K., Clark, M.K., West, A.J., Zekkos, D., Li, G., Gallen, S.F., Chamlagain, D. and Godt, J.W., 2018. The size, distribution, and mobility of landslides caused by the 2015 Mw7. 8 Gorkha earthquake, Nepal. Geomorphology, 301, pp.121-138.

Reid, M.E., Brien, D.L., LaHusen, R.G., Roering, J.J., De La Fuente, J. and Ellen, S.D., 2003. Debris-flow initiation from large, slow-moving landslides. *Rickenmann, D., and Chen, C.-l., eds., Debris-Flow Hazards Mitigation: Mechanics, Prediction, and Assessment, Volumes*, *1*, pp.155-166.

Rosen, P.A., Gurrola, E., Sacco, G.F., Zebker, H., 2012. The InSAR scientific computing environment, in: EUSAR 2012; 9th European Conference on Synthetic Aperture Radar. Presented at the EUSAR 2012; 9th European Conference on Synthetic Aperture Radar, pp. 730–733.

Wang, G., Suemine, A., & Schulz, W. H. (2010). Shear-rate-dependent strength control on the dynamics of rainfall-triggered landslides, Tokushima Prefecture, Japan. *Earth Surface Processes and Landforms*, *35*(4), 407-416.

McAdoo, B. G., Quak, M., Gnyawali, K. R., Adhikari, B. R., Devkota, S., Rajbhandari, P. L., and Sudmeier-Rieux, K.: Roads and landslides in Nepal: how development affects environmental risk, Nat. Hazards Earth Syst. Sci., 18, 3203–3210, https://doi.org/10.5194/nhess-18-3203-2018, 2018.

Zekkos, D., Clark, M., Whitworth, M., Greenwood, W., West, A. J., Roback, K., et al. (2017). Observations of Landslides Caused by the April 2015 Gorkha, Nepal, Earthquake Based on Land, UAV, and Satellite Reconnaissance. Earthq. Spectra 33, S95–S114. doi:10.1193/121616EQS237M.

Zhang, Q., J. Wang, X. Peng, P. Gong, and P. Shi (2002), Urban built-up land change detection with road density and spectral information from multi-temporal Landsat TM data, Int. J. Remote Sens., 23(April 2014), 3057–3078, doi:10.1080/01431160110104728.

Zhao, B. (2016). April 2015 Nepal earthquake: observations and reflections. *Natural Hazards*, *80*(2), 1405-1410.